Annular Modes in a Multiple Migrating Zonal Jet Regime

by

Cegeon J Chan

B.S., Meteorology; B.S. Mathematics
Lyndon State College, 2003

Submitted to the Department of Earth, Atmospheric, and Planetary Science
in Partial Fulfillment of the Requirements for the Degree of

Master of Science in Atmospheric Science

at the

Massachusetts Institute of Technology

February 2006

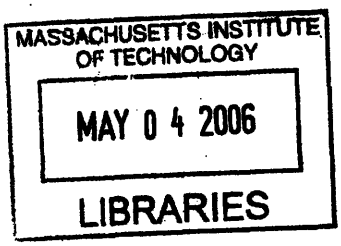

ARCHIVES

Signature of Author.....

Department of Earth, Atmospheric, and Planetary Science
January 25,2006

Certified by.....

R. Alan Plumb
Professor of Earth, Atmospheric and Planetary Science
Thesis Supervisor

Accepted by.....

Maria T. Zuber
E.A. Griswold Professor of Geophysics
Head, Department of Earth, Atmospheric and Planetary Sciences

Annular Modes in a Multiple Migrating Zonal Jet Regime

by

Cegeon J Chan

Submitted to the Department of Earth, Atmospheric, and Planetary Science
on January, 25, 2006, in partial fulfillment of the
requirements for the degree of
Master of Science in Atmospheric Science

Abstract

Recent studies have linked hemispheric climate variability to annular modes, zonally symmetric structures that describe the horizontal redistribution of atmospheric mass. The resulting changes in the pressure patterns consequently alter the atmospheric circulation, including the movement of zonal jets in the atmosphere. While the literature contains much observational evidence describing these annular modes, the fundamental dynamics in the perpetuation of the annular modes still remains poorly understood.

We investigate the dynamics of the annular modes using the MITGCM, a semi-hemispheric ocean model. The forcings imposed in the model are an atmospheric wind stress and relaxation to a latitudinal temperature profile, which induces a baroclinically unstable flow. Despite such an idealized setup, the model output shows striking similarities to the observed atmospheric annular modes, where the leading mode of variability is associated with the primary zonal jet's meridional displacement. By convention, when the zonal jet is poleward (equatorward) of its time-mean position, the principal component (PC) of the first empirical orthogonal function (EOF) is positive (negative) and is referred to as the high (low) zonal index.

In the model, systematic secondary (weaker) jets migrate equatorward into the primary jet. The total eddy forcing associated with the migrating jets aids in sustaining the primary jet in the presence of frictional forces. Plots of the anomalous eddy fields for both indexes show that the strongest eddy activity in the main jet is associated with the high zonal index. The zonal flow anomalies, which systematically migrate into the poleward flank of the main jet, are largely responsible for causing this positively anomalous eddy forcing. This asymmetrical forcing to the primary jet results in the zonal index variability.

In this thesis, the dynamics associated with the secondary jets and its equatorward migration will be examined. We will show that when (1) the sphericity of the earth is accounted for, (2) the interior PV is homogenized, and (3) the width of the baroclinically unstable region exceeds the Rhines scale by several factors, multiple zonal jets emerge and migrate equatorward.

Thesis Supervisor: R. Alan Plumb
Title: Professor of Meteorology

Acknowledgments

Particularly at an university like MIT, graduate programs are setup to test and challenge the students' ability to perform independently. However, one cannot earn a degree without the support from others. The following are the people who have helped me along the way.

First, I would like to thank my advisor, Alan Plumb for frequent insightful discussions. He has helped guide me through my wrong turns and helped me stay on the right course. Despite his busy schedule, I appreciate his ability to always find time for me.

My fellow classmates have always been friendly and have supported the last couple of years. In particular, I would like to thank Yang Zhang, Daniel Enderton, Ian Fenty and Bhaskar Gunturu for our Friday afternoon sessions in the Spring of 2005 working together to prepare for the dreaded General Exam. Their help made the process less daunting. Also, my officemates – Dave Flagg, Vikram Khade, and Kelly Klima – were pleasant to talk with when a break from work was in order.

This thesis would not be possible without the people in my research group – Will Heres, Nikki Privé, Mike Ring, and Ivana Cerovecki. Nikki was my "mentor" and was an excellent resource for advice as a first-year graduate student. Mike provided useful comments that benefitted this thesis, and Ivana always had an answer for any question I had pertaining to the model output and to the MITGCM itself.

Outside of this department, a special thanks go to Jason Furtado and Vivian Cheng. As a friend and colleague from our undergraduate days and now graduate school, Jason has not only helped contribute insightful comments to this thesis, but I have also benefitted from

many fruitful discussions about a variety of topics in our field. Finally, Vivian Cheng, my girlfriend of seven years, has had to put up with the roller coaster ride associated with being a graduate student and its time constraints. She has always been right beside me and been able to provide balance to my often idealistic views of the world with much needed practical perspectives.

This material is based upon work supported by the National Science Foundation under Grant No. 0314094. Any opinions, findings, and conclusions or recommendations expressed in this material are those of the author and do not necessarily reflect the views of the National Science Foundation. Lastly, I also acknowledge the financial support from the NASA's Earth Science Enterprise Graduate Fellowship.

Contents

List of Figures

Chapter 1

Introduction

1.1 Annular modes

Modes of climate variability in the atmosphere have long been studied. Calling it the North Atlantic Oscillation (NAO), Walker and Bliss (1932) demonstrated negative correlations in pressure between the North Atlantic and the subtropics of Europe. Meanwhile, Rossby (1939) introduced the zonal index as a measure of the strength of the mid-latitude westerlies between 35° N and 55° N. Namias (1950) went further by proposing the fluctuations in the flow strength was associated with the "zonal index cycle," an oscillation owing to the jet's meridional displacement. Lorenz (1951) then linked the two latter ideas together by averaging the zonal-mean zonal flow at 55°N and using it as a proxy to measure the pressure oscillation.

In more recent years, Thompson and Wallace (1998), who first used the term "annular modes", described the leading mode of variability as a seesaw of mass between mid- and

high-latitudes similar to Walker and Bliss (1932). However, Thompson and Wallace (1998) expanded the regional analysis to include the entire hemisphere. They showed that there was a stronger connection between the variability of the wintertime Eurasian surface air temperatures with the leading mode of the hemispheric zonal-mean sea-level pressure rather than to the regional fluctuations associated with the NAO. Furthermore, other studies (e.g. Limpasuvan and Hartmann 2000) have demonstrated that this leading mode of variability is not only annular-like, but is barotropically equivalent, i.e. the pattern extends from the surface up to the tropopause and amplifies with height.

Although annular modes are observed in both hemispheres, Lorenz and Hartmann (2001), hereafter LH01, analyzed the Southern Hemisphere (SH) annular mode (SAM) which is more zonally symmetric and provides more robust results than its northern counterpart. They showed that anomalously high pressure in the mid-latitudes is associated with a poleward shift of the jet and, conversely, anomalously low pressure in the mid-latitudes is associated with an equatorward shift of the jet. By convention, a poleward shift of the jet corresponds to a high index phase while an equatorward shift is defined as a low index phase.

Lorenz and Hartmann (2001) described the jet displacement as the leading mode of zonal-mean zonal flow variability through the first empirical orthogonal function (EOF) of $[u]$. Its dipole structure, with local maximum and minimum anomalies centered about ten degrees north and south of the time-averaged maximum wind speeds, captures the "wobbling" or meridional displacement of the zonal jet. The second EOF coincided with the location of the mid-latitude jet representing the strengthening and weakening of the jet, or similarly the

jet narrowing and broadening of the jet.

The time-scales associated with these modes can range from intra-seasonal to decadal (Thompson and Wallace 1998). Therefore, annular modes can be helpful to describe climate change. For example, Hurrell (1995) showed a strong correlation with surface air temperature with the annular modes over the previous 30 years. Thompson and Wallace (2000) also show that the Northern Annular Mode (NAM) index trended toward a persistent positive phase in the late 1980s and throughout the 1990s, consistent with trends in the NAO (e.g. Hurrell 1995).

1.2 Zonal Jets

The reasoning behind examining ring-like structures for low-frequency behavior can be attributed to many processes. But primarily, based on the theories of geostrophic turbulence in barotropic fluids and conservation of energy and enstrophy, kinetic energy is transferred from high wave numbers to low wave numbers, while enstrophy cascades from low wave numbers to high wave numbers, where it dissipates (Pedlosky 1987). The effect of the inverse energy cascade creates spatially larger eddies. In the absence of other forces such as rotational and frictional forces, eddies will grow to the size of the domain.

Rhines (1975) described how the β-effect can halt the cascade of energy to larger scales. As the eddies grow in size, variations of planetary vorticity increase in importance, and when eddies are sufficiently large, the effect of Rossby wave dynamics will be approximately equal to nonlinear interactions. From the barotropic vorticity equation shown below, a scaling

argument shows the length scale at which a turbulent regime turns more dynamically wave-like.

$$\frac{\partial \zeta}{\partial t} + \vec{u} \cdot \nabla \zeta + \beta v = 0 \tag{1.1}$$

where ζ is the relative vorticity, $\vec{u}$ is the velocity, and v the meridional speed.

The second term scales as $\frac{U^2}{L^2}$ and the third term scales as βU. For small scales, the advective term dominates, and for large scales, the β-term dominates. When the two terms are in "balance", it is called the Rhines scale:

$$L_\beta \sim \sqrt{\frac{U}{\beta}} \tag{1.2}$$

In the meridional direction, the Rossby wave frequency is inherently anisotropic, therefore flows organize themselves into zonal structures (Rhines 1975). This can be attributed to the general tendency for the energy to seek the gravest mode and hence cascade toward low zonal wavenumbers (Vallis and Maltrud 1993). In essence, this process "flattens" the eddies in the north-south direction and turns them from isotropic to anisotropic. Therefore, the final process of the cascade leads to longitudinally oriented eddies producing zonally symmetric jet-like flows (Rhines 1975).

Adjusting to a baroclinically unstable regime, Held and Larichev (1996) used a scaling argument to come up with an adjusted "baroclinic" version of the Rhines scale, $\hat{k}_\beta = \frac{\beta L_D}{\hat{u}}$, where $\hat{u}$ is the baroclinic eddy velocity and L_D is the baroclinic Rossby radius of deformation. Therefore, if the domain size is larger than this scale, the possibility for more than one

zonal jet can exist. Furthermore, numerical studies (e.g. Williams 1978) have shown if the baroclinically unstable region greatly exceeded the Rhines scale, multiple jets develop.

Panetta (1993) imposed an unstable horizontally uniform vertical shear over several tens of Rossby radii wide with a quasi-geostrophic (QG) two-layer β-plane model to test for the existence of multiple jets. Given dissipation was sufficiently weak, multiple jets emerged and were demonstrated to be remarkably persistent. By using a full zonal and meridional spectrum, Panetta (1993) also showed the existence of multiple jets was not a consequence of leaving out long zonal waves i.e. low model resolution did not lead to fabrication of zonal jets.

Panetta recognized the earth's ocean, where the Rossby radius of deformation is an order of magnitude smaller than the atmosphere, would allow for multiple jets to be observed e.g. the Antarctic Circumpolar Current (ACC). Using a QG channel model forced by a surface wind stress, Treguier and Panetta (1994) found multiple jets would emerge given a limited amount of curvature to the meridional wind stress.

These numerical studies by Williams (1978), Panetta (1993) and Treguier and Panetta (1994) were all done using a quasi-geostrophic (QG) model. Expanding upon the hierarchy of models simulating multiple jets, Lee (2005) utilized a primitive equation model on a spherical planet. Varying the size of the planetary radius and baroclinic intensity, Lee demonstrated the meridional scale of the jet was consistent in each case with the Rhines scale.

1.3 Motivation

The above studies of multiple jets have been based on simplified models such as QG models on a β-plane. Only through modelling multiple jets with different levels of model complexity can theories be rigorously tested. Our use of the MITGCM serves multiple purposes. Since the MITGCM uses spherical coordinates, the model captures the earth's latitudinal variations of the earth's curvature. It can be shown that the group velocity is proportional to eddy momentum fluxes (Andrews et al. 1987). Therefore, Rossby waves have a bias in propagating equatorward (e.g. Whitaker and Snyder 1993; Limpasuvan and Hartmann 2000). Under this framework, this will lead to asymmetric forcing in relation to the zonal jet that models using a β-plane omit.

This work was primarily motivated by the output from a ocean model run from the MITGCM. Similar to previous studies, the setup is such that width of the baroclinic region is much larger than the baroclinic Rossby radius of deformation. However, secondary (weaker) jets are observed to systematically migrate equatorward. The author is not aware of such behavior being reported previously. Since the model-imposed forcings are constant in time with flat-bottom topography, it is the internal dynamics most likely responsible for establishing the remarkable persistence of the migrating zonal jets. This equatorward bias in the zonal anomalies is in contrast to the poleward propagation of the zonal anomalies observed in the atmosphere (Feldstein 1998).

Along with addressing this issue, another goal of this work is to describe and explain the annular mode-like behavior associated with this model run. The leading mode of variability of

the zonally-averaged zonal flow describes the meridional displacement of the primary jet, very similar to the observed atmosphere (e.g. Lorenz and Hartmann 2001). The model-imposed forcings here are constant in time, but yet, there is still temporal variability associated with the zonal jets. The most likely explanation can be attributed to the eddy effects on the zonal-mean flow.

Yu and Hartmann (1993) conducted a modelling study with a GCM and determined the convergence of the transient eddy momentum flux is important in not only maintaining a meridionally displaced jet, but also in the transition from one zonal index to another. This implies a momentum budget analysis is important to show that the eddy momentum flux convergence is the major forcing in both the extreme and transitional phases. It would be of interest to compare eddy statistics given our regime of migrating jets.

We note that the two forcings to the model have been idealized. The model-imposed wind stress does not account for easterlies in the tropical atmosphere, i.e. there are only westerlies in mid-latitudes and the wind stress tapers off equatorward. The requirements needed for such conditions (if even plausible) will not be discussed here. However, a cursory description of the model will be presented in section 2, and in section 3, we will perform a time-average of certain diagnostics in order to examine the climatology of the model. Then, we will analyze the spatial and temporal variability by utilizing empirical orthogonal functions (EOFs) in section 4. Descriptions of the eddy properties will be presented and discussed in section 5. In section 6, a comparison will be made between some our GCM results and simple models. A discussion on our results will be given in section 7. Finally, we conclude with a summary

of our important findings and discuss potential future work in section 8.

Chapter 2

Setup

2.1 Model

The data in this study were generated from the MIT General Circulation Model (MITGCM). A more complete description of the MITGCM can be found in Marshall et al. (1997a, 1997b). Here we provide just a cursory description of the model setup.

This is a semi-hemispheric model ranging from 50.67°S to 0.17°S and 0°E to 10° E periodic in the zonal direction on a $\frac{1}{6}^{\circ} \times \frac{1}{6}^{\circ}$ latitude/longitude grid. There are 15 vertical layers with each layer's depth ranging from approximately 22m in the first top six layers to approximately 400m for the bottom nine layers. A two-dimensional sketch is shown in Figure 2.1.

The simulated ocean varies from the actual ocean in a number of ways. Boundaries such as continents and topography that could potentially influence the flow have been ignored. The model does not account for trade winds, i.e. only westerlies with the wind tapering off

towards the equator are considered.

In the absence of such boundaries, the model has been setup to be a zonally reentrant channel. The periodic boundary conditions in the zonal direction are, in general, more representative of the atmosphere than the ocean and may facilitate annular mode-like structure similarly observed in the atmosphere. However, unlike the atmosphere, the fluid is channelled between two walls. Free-slip and no-slip boundary conditions are used at the equator and at 50.5°S, respectively.

The model-imposed forcings include a wind stress (Figure 2.2a) and a heat forcing (Figure 2.2b). Both forcings are constant in time, a function of latitude only, and applied only to the top layer of the ocean. Compared with the oceanic Rossby radius of deformation (which is in the order of 50 km), the width of the forcings are extremely broad.

For our oceanic case, this wind stress acts as our source of momentum from the atmosphere into the ocean's top layer, with the peak located at 33°S. When the model starts integrating, the wind stress will cause the top layer's zonal flow to increase with time. After a sufficient length of time, the flow becomes baroclinically unstable, perturbations grow, and eventually, eddies transfer momentum equatorward and downward, until eventually momentum is then removed out of the system at the ocean's bottom due to bottom drag.

The second applied forcing is a model-imposed temperature profile. The restoring time for this heat forcing, shown in Figure 2.2b, to return to the specified temperature profile is of order 1 month. Thus this heat forcing is associated with warming close to the equator and cooling to the south. This semi-realistic forcing is also constant in time and independent of

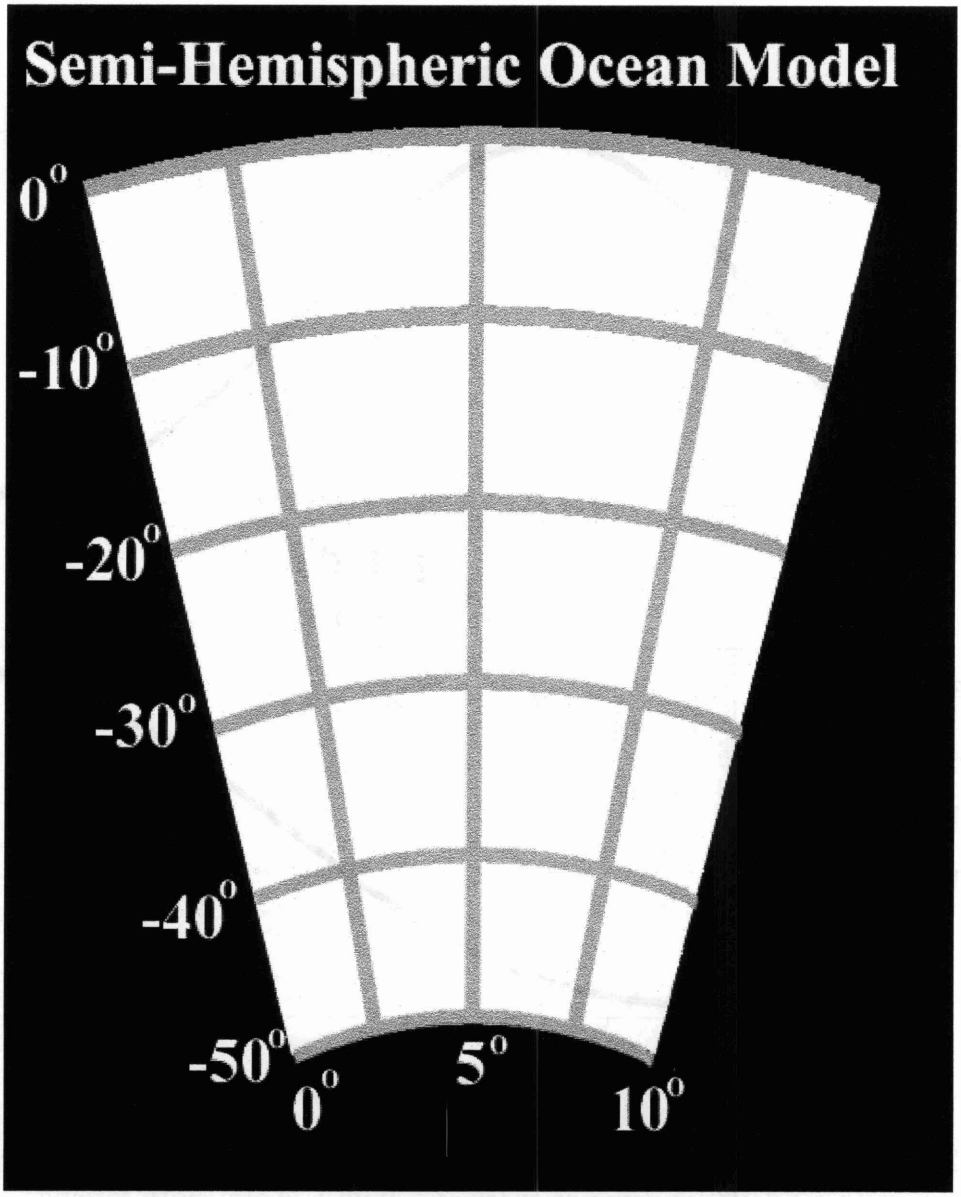

Figure 2.1: Model's domain ranges from 50.67°S to 0.17°S and 0°E to 10° E and periodic in the zonal direction on a $\frac{1}{6}^\circ \times \frac{1}{6}^\circ$ latitude/longitude grid. See text for details.

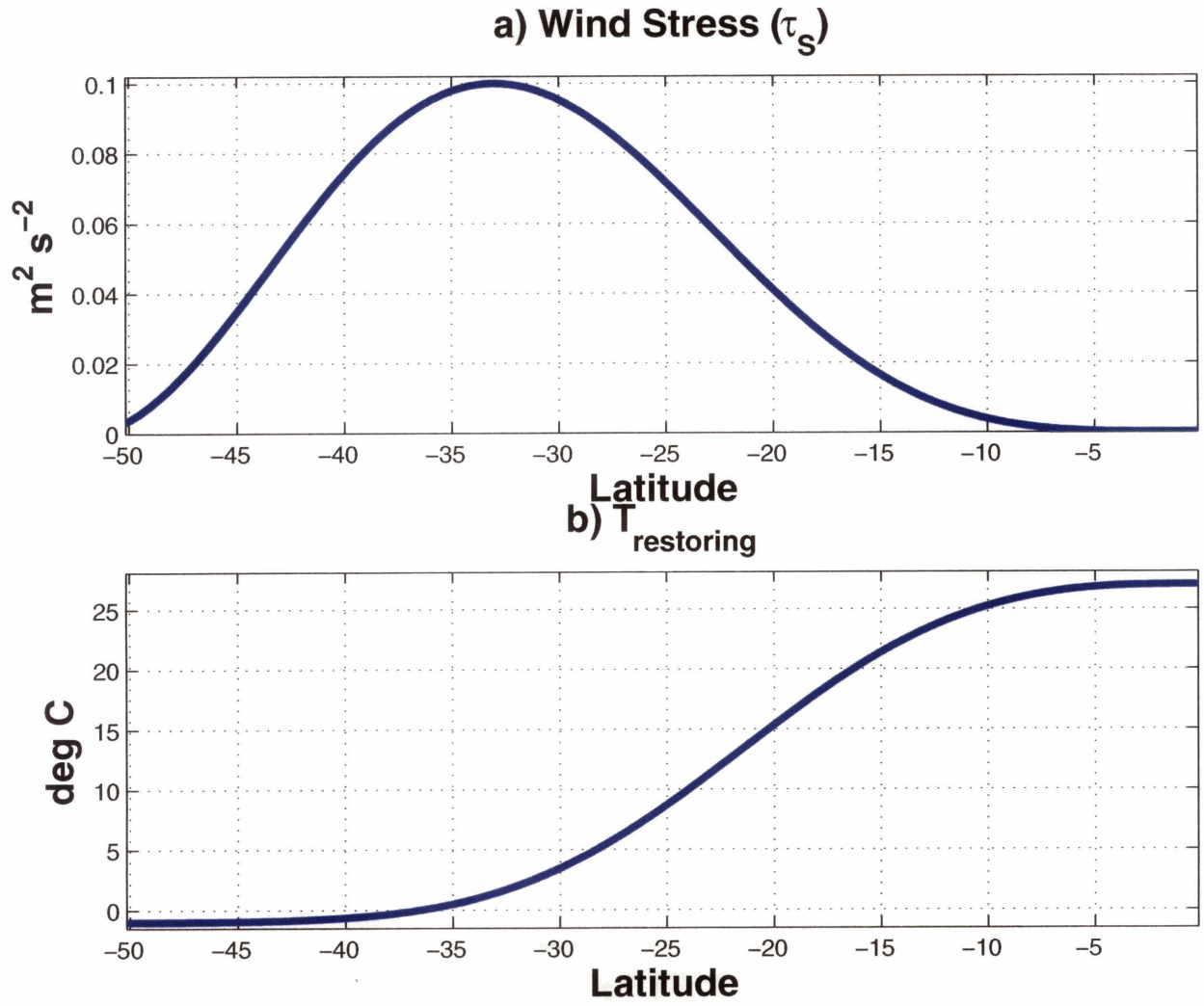

Figure 2.2: Model-prescribed forcings. (a) Atmospheric wind stress. (b) Specified temperature profile with a relaxation time of order one month. Note: both forcings are constant in time, only a function of latitude, and applied to the top surface layer (22m).

longitude.

The size of any eddies is always limited to size of the particular model's domain. Part of the model's domain size is shown in Figure 2.3. In certain parts, the 10° width of the channel likely stopped the inverse energy cascade. Between 12°S and 17°S, an eddy fills the entire latitude circle and has most of its energy in wave number 1. It is likely if given a sufficiently larger zonal domain, the eddy would have been horizontally larger and appear less isotropic i.e. more zonal as described by Rhines (1975).

The depth of the ocean is 4083m, and the model's bottom drag is specified to be:

$$\tau_{bot} = 2A_z \frac{u_{bot}}{\delta_{bot}} + C_D u_{bot} \sqrt{KE} \tag{2.1}$$

where A_z is the vertical viscosity, u_{bot} is the zonal velocity at the bottom of the ocean, τ_{bot} is the thickness of the bottom layer, KE is the kinetic energy and C_D is the bottom drag coefficient.

2.2 Methodology

With the lack of any longitudinally asymmetric forcing, it is appropriate to consider zonal mean budgets. Therefore, since we are interested in the low-frequency behavior, unless otherwise noted hereafter, quantities displayed in this paper have been annually and zonally-averaged and will be denoted with square brackets.

In the literature, there are many possible definitions of the zonal index. For this study,

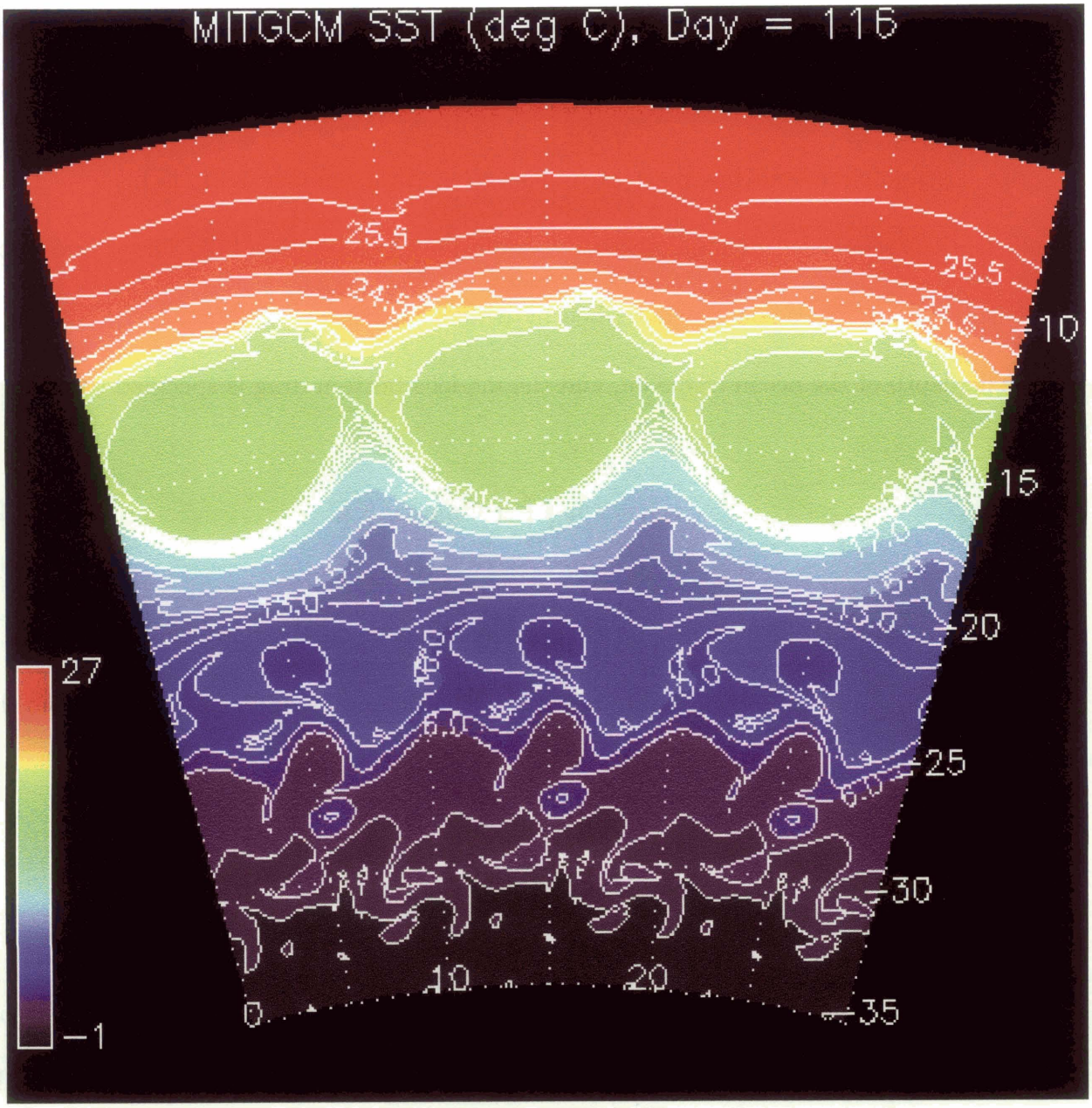

Figure 2.3: Snapshot of the horizontal temperature distribution. For visual purposes, since the model is periodic in the zonal direction, the graphical output between 10° and 30° are duplicates of that for 0 - 10°.

we use the principal component (PC) of the leading empirical orthogonal function (EOF) of the zonally-averaged zonal flow to define the "zonal index." As we shall see, the first EOF describes the north-south displacement of the jet. Positive (negative) values of the PC indicate a poleward (equatorward) shift of the jet and will be referred to as a high (low) phase of the zonal index.

Figure 2.4 displays the time series of the annually and zonally-averaged flow over a nine-year period. The flow is strongest between 15°S and 20°S and closest to the surface with peak values approximately 2.5 ms^{-1}. Poleward of 20°S, weaker zonal jets develop around 35°S and migrate equatorward. The zonal jet between 15°S and 20°S will be referred to as the primary jet, and zonal jets poleward of 20°S will be called secondary jets.

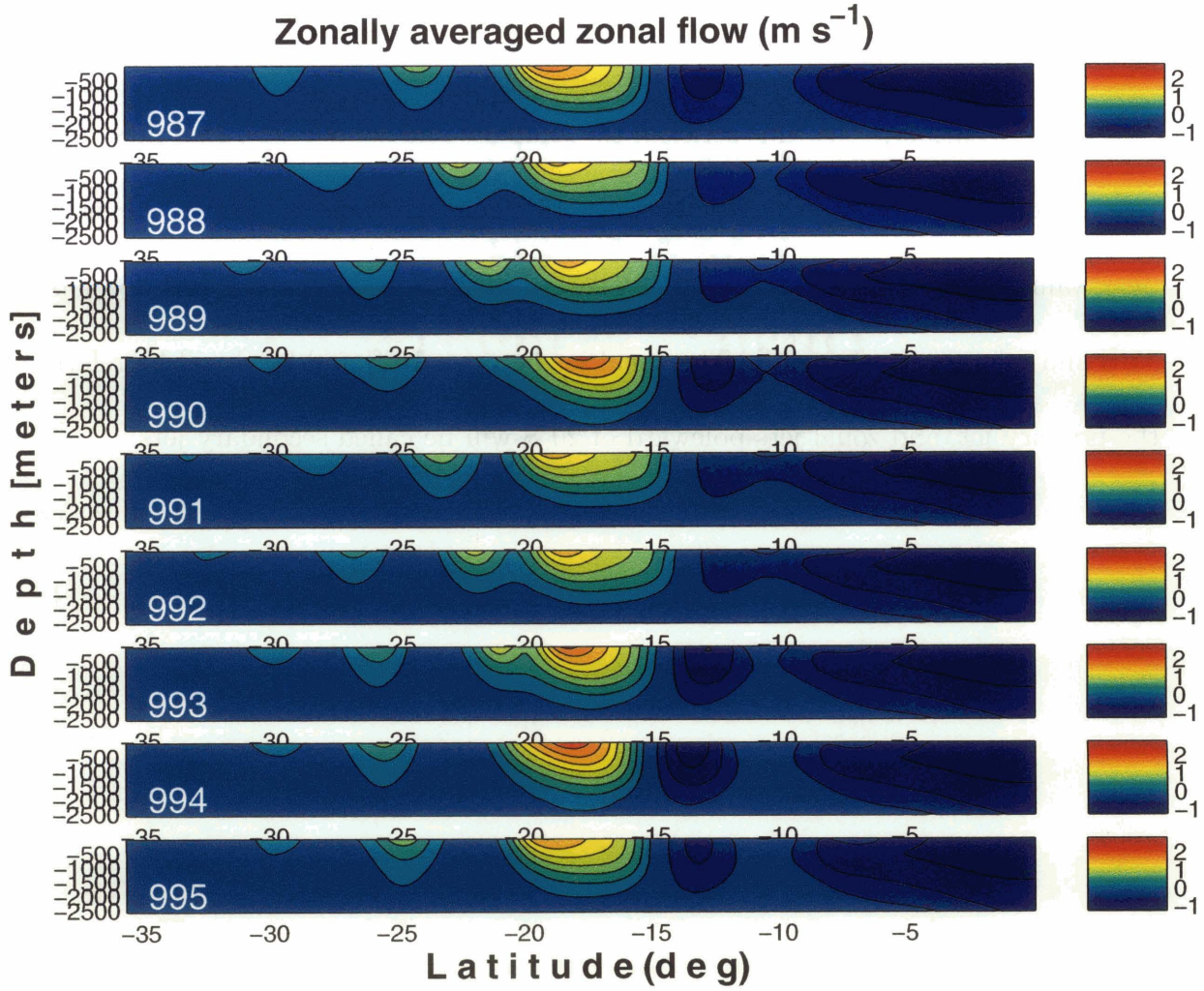

Figure 2.4: Time series of $[u(y, z, t)]$. Time stamps (in years) are located on bottom left corner of each plot.

Chapter 3

Climatology of the MITGCM

The 313-year time series of the zonal-mean zonal flow $[u(y, z, t)]$ shown in Figure 2.4 can be split into two parts: the time mean $[\bar{u}(y, z)]$ and its deviations, $[u'(y, z, t)]$. In this section, we focus on the former. The top plot of Figure 3.1 shows the latitude-depth plot of the zonal-mean zonal flow. This time-averaged plot shows the highest zonal flow values located between 15°S and 20°S, with the primary jet centered at 17°S. Poleward of this primary jet, time-averaged zonal flow speeds appear to be about an order of magnitude less. As shown in Figure 2.3, the period for secondary jets migrating into the primary jet is approximately 10 years. Therefore, because of the migrating jets, such a long time-average (313 years) smooths out the zonal flow south of 20°S. Nevertheless, there is still a hint of another zonal jet at 27°S.

The mean meridional temperature gradient, shown in the second plot of Figure 3.1, has its largest values coinciding with the strong jet as expected by thermal wind balance. The meridional temperature gradient extends through the vertical, damping as we progress

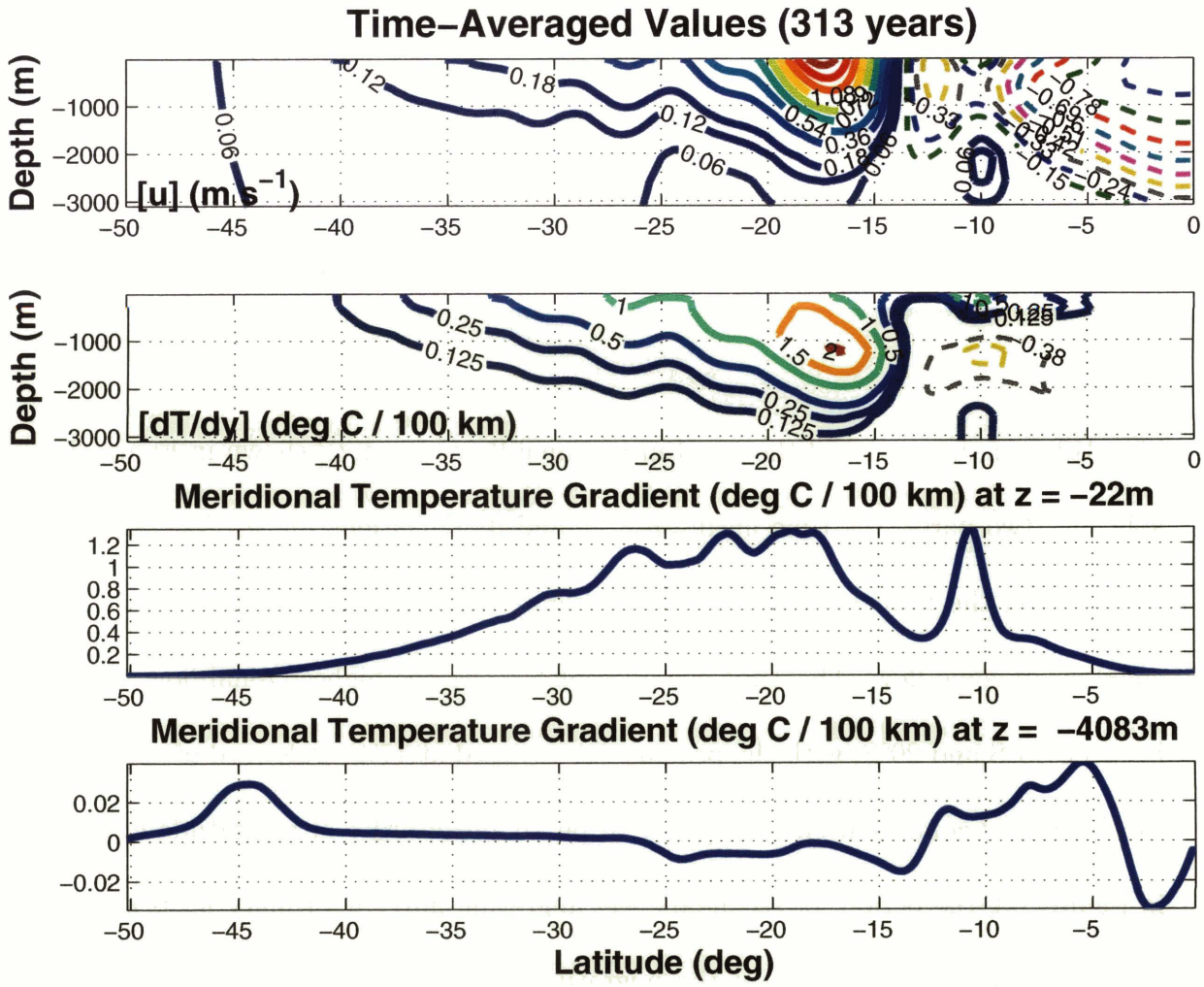

Figure 3.1: Model's time and zonally-averaged values for (a) zonal flow, (b) meridional temperature gradient, (c) meridional temperature gradient at the top boundary and (d) lower boundary.

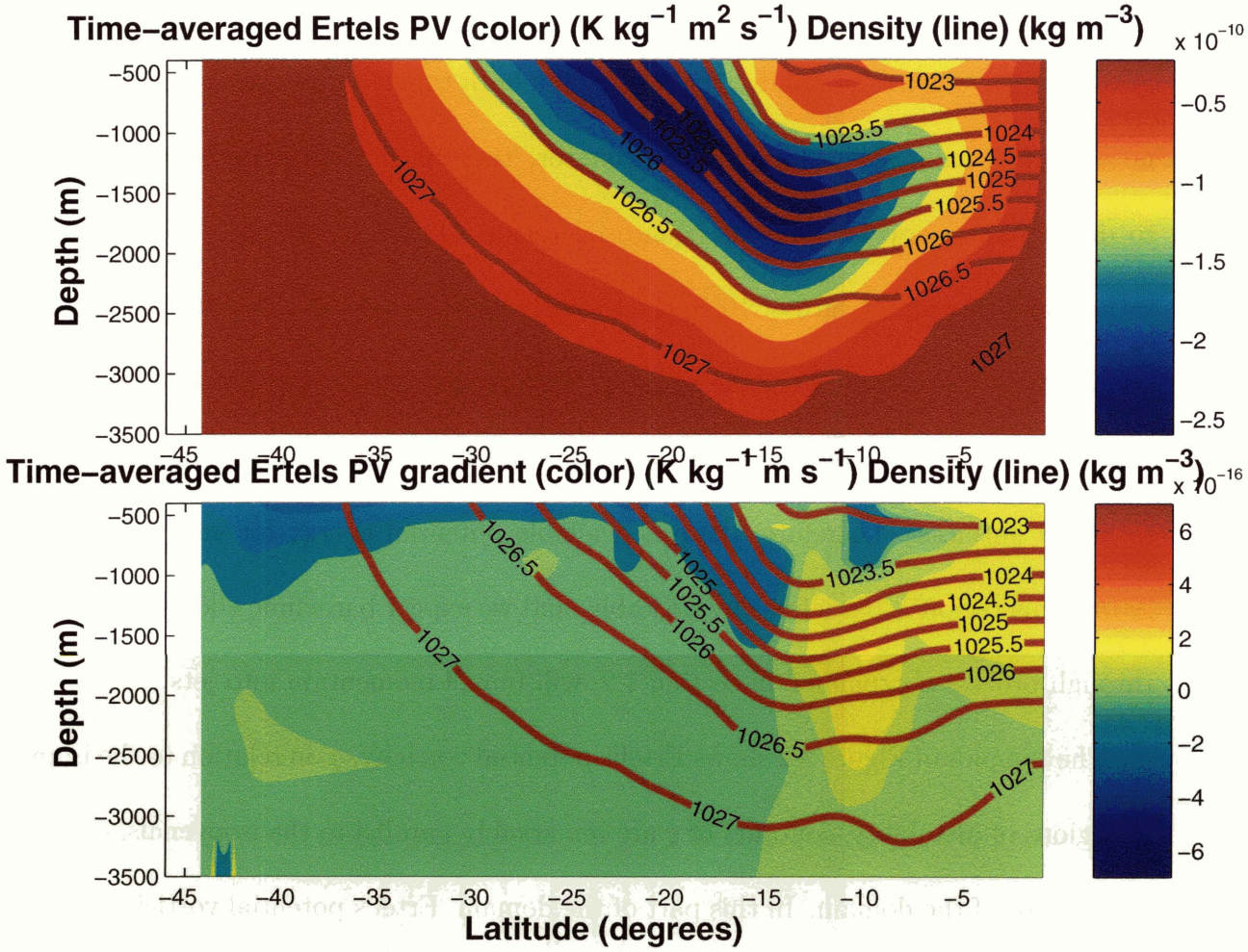

Figure 3.2: Model's time and zonally-averaged values for Ertel's potential vorticity (top) and its meridional gradient (bottom) along isopycnals.

downward, consistent with an equivalent barotropic structure. This implies that the $\frac{\partial T}{\partial y}$ have the same sign along the top and bottom boundaries as shown in Figures 3.1c and 3.1d between 50.5° and 26°S and violates the Charney-Stern sufficient condition for stability. However, this is not the most obvious way to examine the system's stability.

In Figure 3.2, Ertel's potential vorticity is plotted along with lines of constant density. First focusing on the isopycnals, they are relatively flat equatorward of 14°S, and therefore,

one would expect this region to be stable. This is consistent with the applied wind and heat forcings (Figure 2.1a and 2.1b) as they are both tapered off towards the equator. With no westward wind stress towards the equator, there is no upwelling (significant enough) to disturb the isopycnals in this equatorial region. In addition, since the heat forcing is rather smooth equatorward of 10°S, the westerly wind stress was tapered to prevent inertial instability and upwelling near the equator. This region, equatorward of 10°S, is stable.

Poleward of 14°S, the time-averaged isopycnals have significant slopes with comparison to height surfaces. Therefore, there is available potential energy for any perturbations to grow. This region is baroclinically unstable, and we expect baroclinic eddies to develop, and through processes explained in section 1.2, will funnel momentum into jets.

The top plot of Figure 3.2 shows Ertel's potential vorticity, q, in relation to the isopycnals. In regions of instability, contours of q are remarkably parallel to the isopycnals, especially in the interior of the domain. In this part of the domain, Ertel's potential vorticity has become homogenized along the time-averaged isopycnals. The likely mechanism in smoothing q can be attributed to eddies transporting PV downgradient (see Rhines and Young 1982; Kuo et al. 2005). The bottom plot emphasizes the point that Ertel's PV gradient (along isopycnals) is virtually zero in the interior.

The time-mean of the eddy momentum flux is shown in Figure 3.3a and Figure 3.3b. Poleward (equatorward) of the primary jet, momentum is being transferred equatorward (poleward.) Figure 3.3c and Figure 3.3d shows that almost all of the time-mean horizontal momentum flux converges at the primary jet. There is a hint of another convergence

maximum region centered at 27°S where another secondary jet is observed (see Fig 3.1a).

This is consistent with a study done by Held and Andrews (1980). The authors' have shown that flows with a horizontal jet structure broader than the Rossby radius of deformation will have a vertically-integrated momentum flux into the jet. For our study, the Rossby radius of deformation (see Fig 3.4) is on the order of about 100 km, while the primary jet length scale is about 500 km and as shown, in Fig 3.3d, there is a convergence of eddy momentum flux. This is likely to be the mechanism that sustains the jet even in the presence of frictional forces. This will be discussed further in section 5.3.

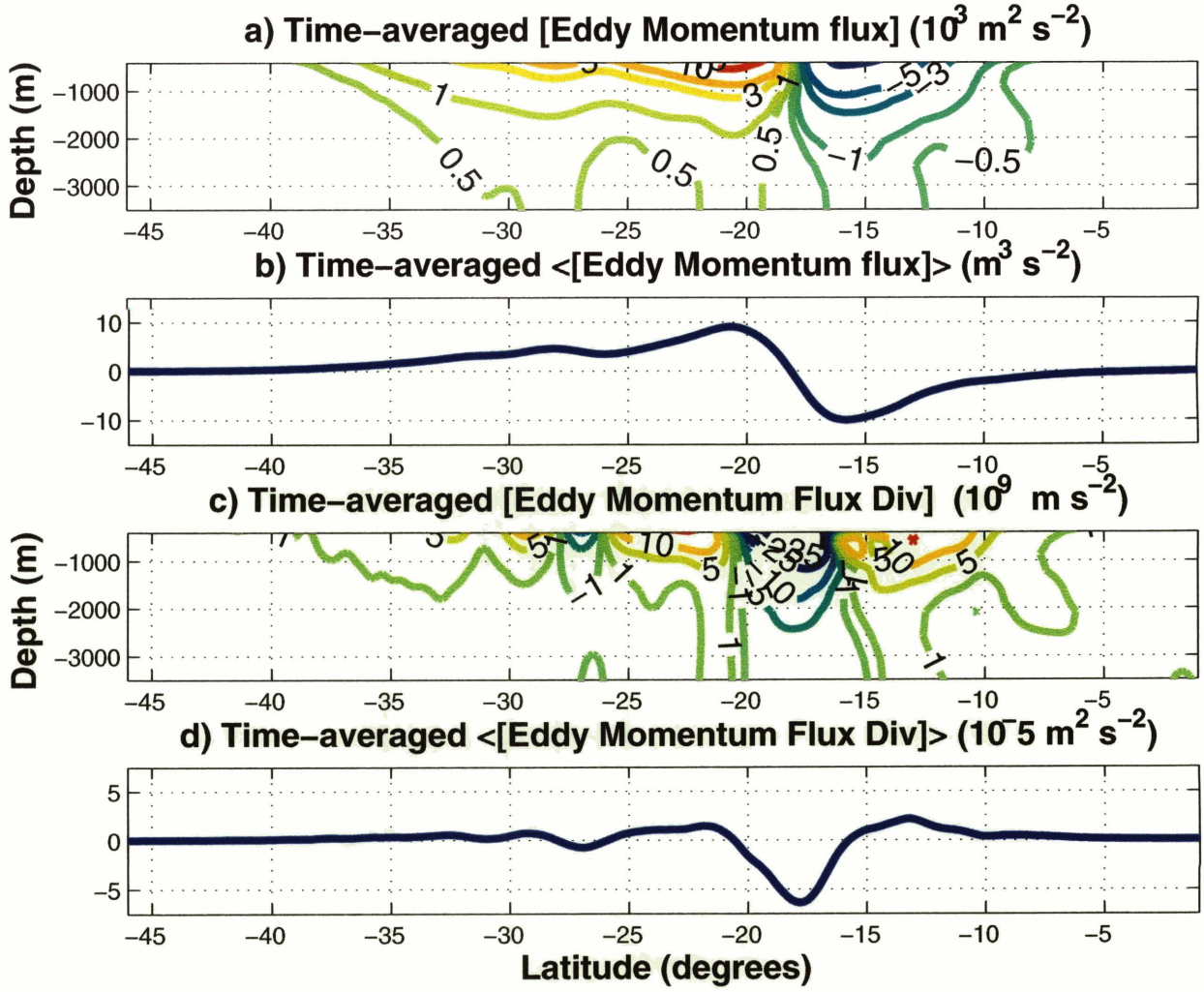

Figure 3.3: Time and zonally-averaged values for (a) the eddy momentum flux (b) vertically-integrated eddy momentum flux (c) eddy momentum flux divergence (d) vertically-integrated eddy momentum flux divergence.

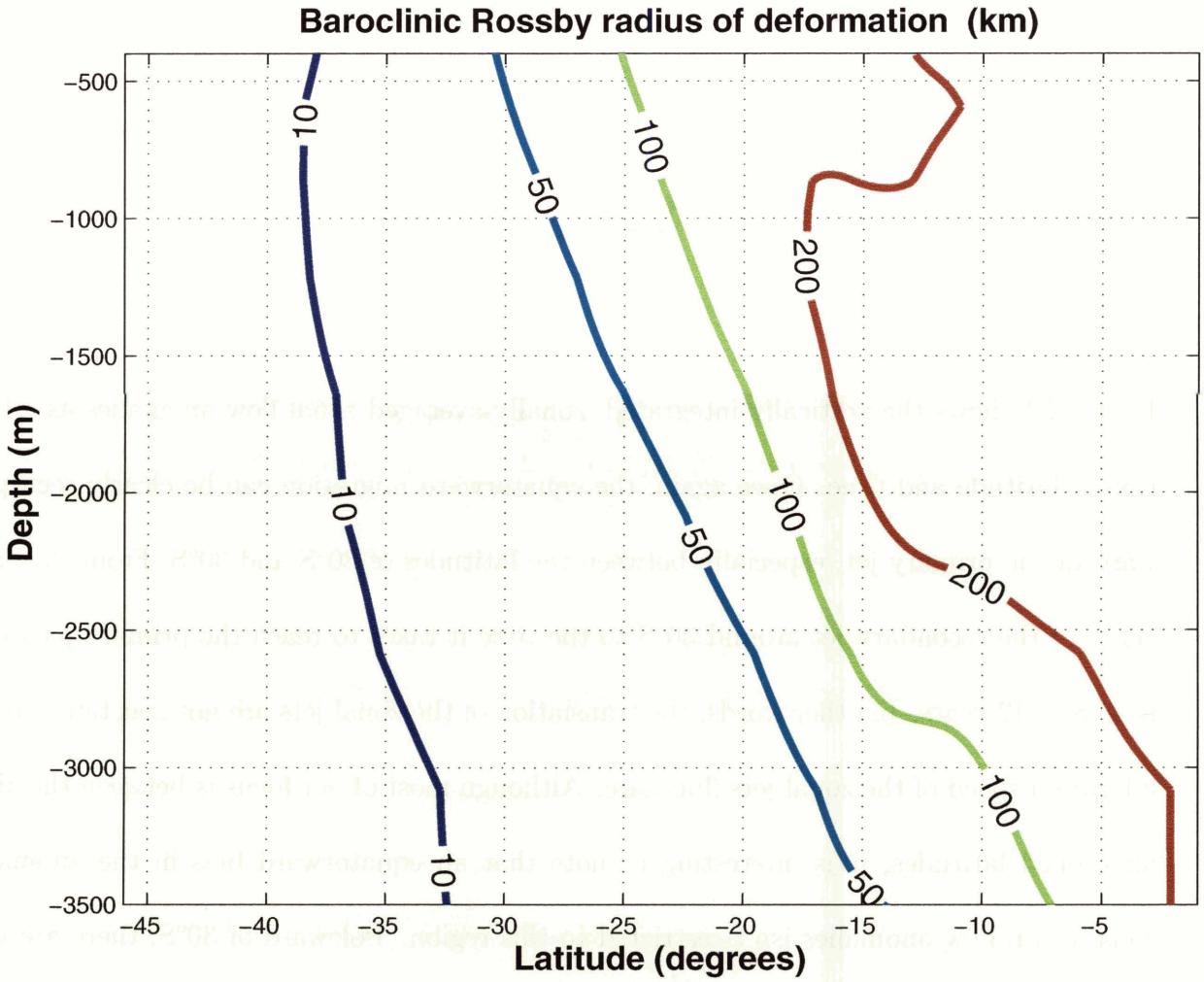

Figure 3.4: Baroclinic Rossby radius of deformation.

Chapter 4

Description of Variability

Figure 4.1 shows the vertically-integrated, zonally-averaged zonal flow anomalies as a function of latitude and time. Once again, the equatorward migration can be clearly seen poleward of the primary jet, especially between the latitudes of 20°S and 30°S. From the emergence of the secondary jet around 30°S to the time it takes to reach the primary jet ranges from 8 to 12 years. In other words, the translation of the zonal jets are not constant, i.e. the migration speed of the zonal jets fluctuate. Although most of our focus is between the above mentioned latitudes, it is interesting to note that an equatorward bias in the anomalous zonal-mean flow anomalies isn't restricted to this region. Poleward of 30°S, there are weak zonal anomalies that also show an equatorward bias and exhibit similar migration speeds as the stronger secondary jets.

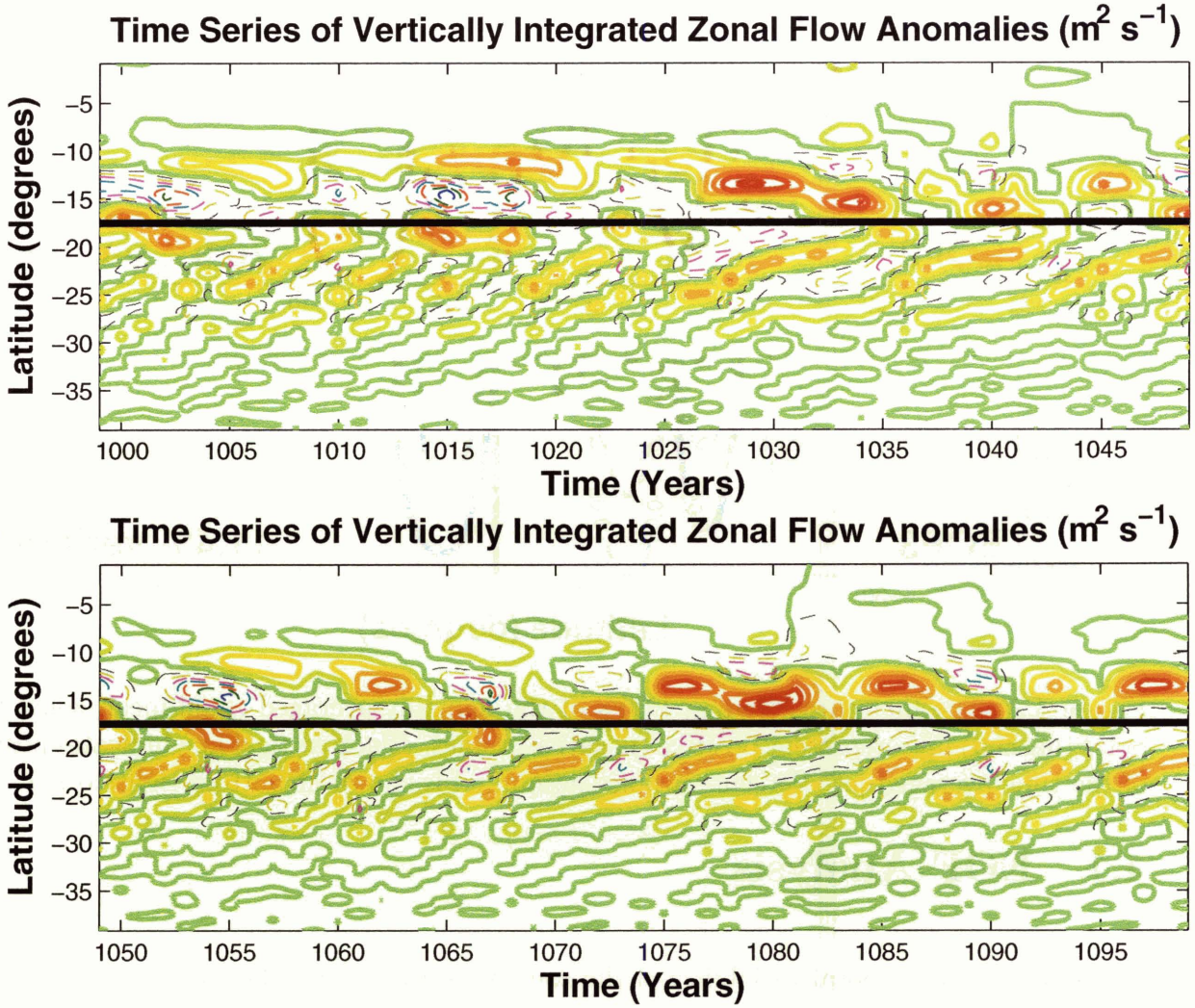

Figure 4.1: Time series of the anomalous vertically-integrated zonally-averaged zonal flow. Positive contours start at 20 and increase in increments of 200. Negative contours (dashed lines) start at -200 and are also in increments of 200.

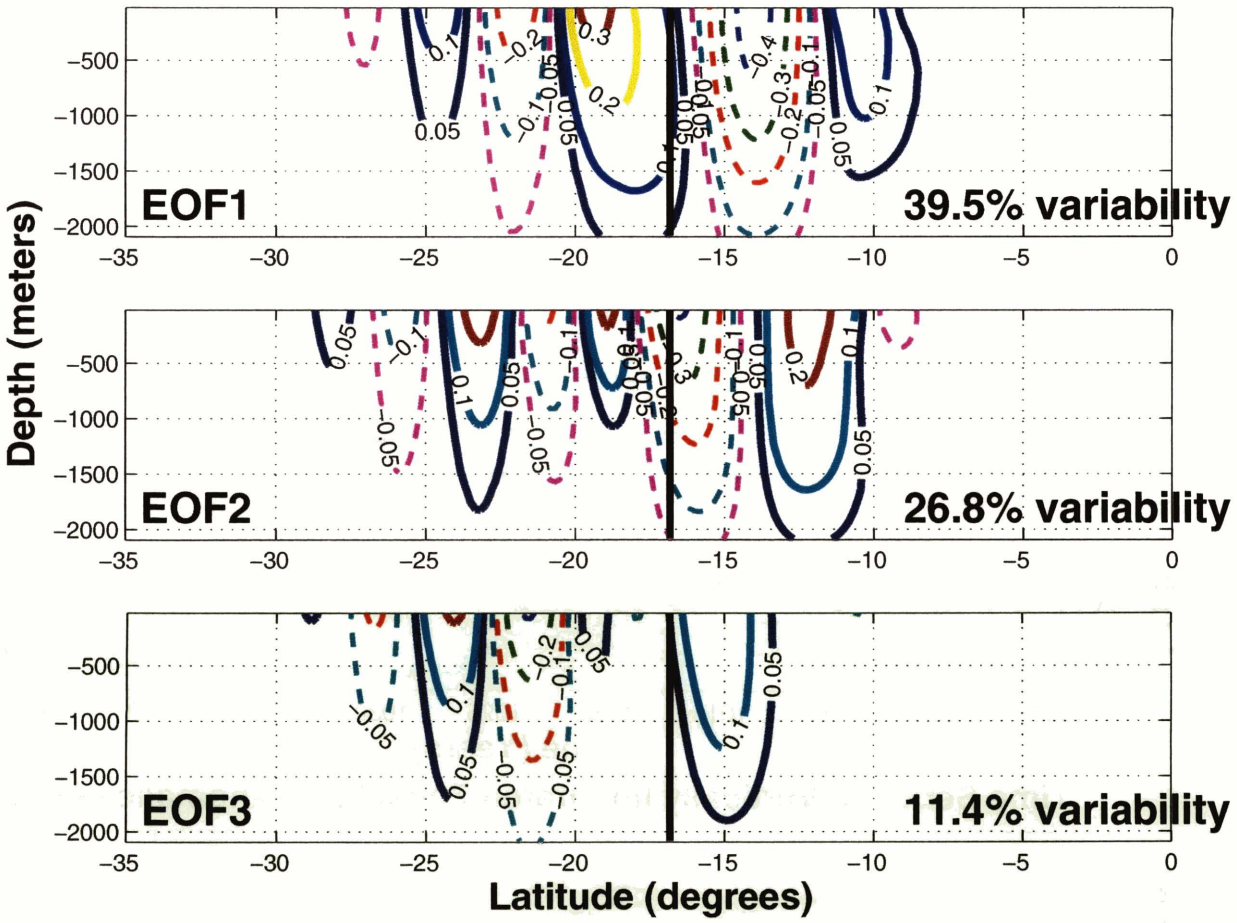

Figure 4.2: The first three leading EOFs of the annually-averaged zonal-mean zonal flow. Solid (dashed) lines represent positive (negative) values. Black vertical line indicates position of the time-averaged jet. Percent variance accounted is shown at bottom right corner.

4.1 EOF Analysis

The spatial and temporal variability of the zonally-averaged zonal flow can be best summarized by the use of empirical orthogonal functions (EOFs) as shown in Figure 4.2. The data was weighted to account for the decrease in area around latitude circles toward the pole, but was not weighted to account for the varying vertical layer depths. However, this shall not be important as we are interested in the horizontal variations of the zonal flow. Using the North et al. (1982) test, the first and second EOFs are-well separated.

EOF1 shows an equivalent barotropic structure with maximum anomalies at 19°S and 14°S. The black line represents the time-averaged location of the jet's maximum value (17.2°S). By comparing the variability of this mode and the mean location of the jet, we determine that EOF1 physically represents the meridional fluctuations of the main jet, or in other words, EOF1 captures the jet "wobbling" in the north-south direction. This mode constitutes the largest amount (39.5 percent) of the total variability.

In EOF2, the maximum anomalies are coincident with the mean location of the jet. Therefore, this mode physically represents the intensifying and weakening of the main jet. With this mode capturing twenty-seven percent of the total variance, EOF1 and EOF2 together account for over sixty-six percent of variability.

These leading modes of variability are robust. A similar spatial pattern develops after splitting the 313 years into different segments (not shown). A plot of the principal component of EOF1 and EOF2 will provide the amplitude, phases, and the duration of the variability associated with each mode ranges . From (Figure 4.3), the duration of EOF1 lasts anywhere from 1-7 years, but typically for 3-4 years and oscillates from positive to negative numbers, indicative of the jet "wobbling" north and south of its time-mean location. For example, this would physically imply that the EOF1 accounts for the primary jet being shifted, while PC1 shows that it persists for about one to six years. Similarly, EOF2 shows that usually the primary jet is anomalously stronger/weaker, while PC2 shows that is lasts anywhere from one to ten years.

To demonstrate how these leading modes capture both the spatial and temporal variabil-

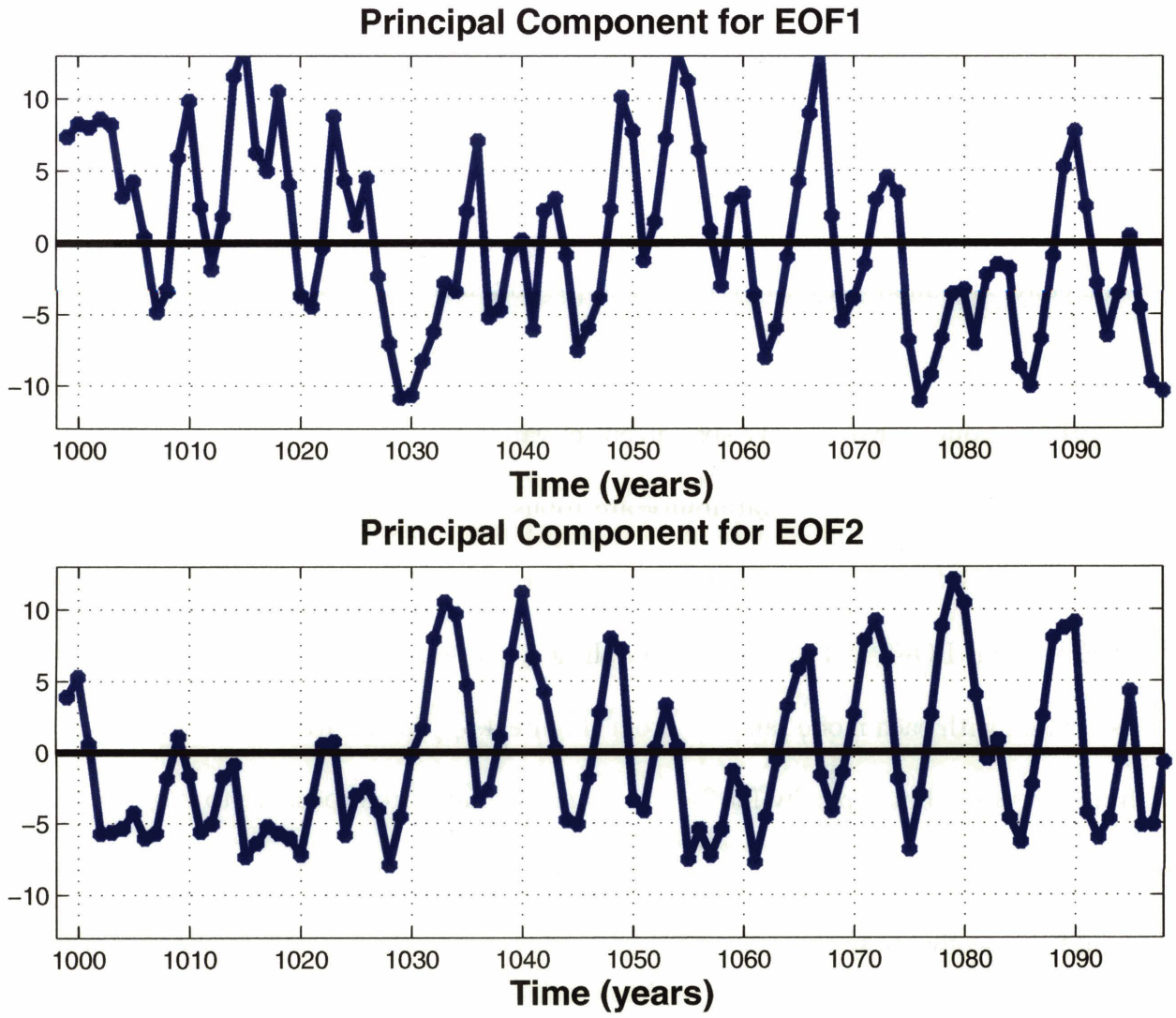

Figure 4.3: Principal components of the first and second EOF modes.

ity, we reconstruct the zonal flow by using just only the first two eigenvectors (for calculations, see Appendix A.) A time series of the reconstructed zonal flow with the two EOFs can be seen in Figure 4.4. Comparing this to Figure 2.4, the reconstructed zonal flow captures the variability from the original data set. More specifically, the migrating jets are preserved. Unsurprisingly, the vertical structure throughout the time series, show the reconstructed zonally- and annually-averaged zonal flow to remain equivalent barotropic. The only difference between the reconstructed zonal flow and the original is that the jets are slightly weaker and shallower in the former and may be the result of not accounting for the different layer depths, which were shallow at the top and deep at the bottom when solving for the eigenvectors. Layers close to the surface were weighted too much, while the bottom layers weighted too little.

4.2 Description of EOF phases

Lorenz and Hartmann (2001) analyzed the zonal-mean zonal wind variability in the Southern Hemispheric atmosphere and found EOF2 (eighteen percent variability) to only account for one-half of what EOF1 captured. For our study, EOF2 accounts for more than two-thirds of what EOF1 captures in the total variability. This demands the anomalous activity associated with the EOF2 spatial pattern to contribute more into the dynamics than in the LH01 study.

A single EOF for the reconstructed $[u]$, would simply describe jets strengthening and weakening, but not migrating. Thus, the need for two EOFs to capture most of the variability make sense since our secondary jets are not just simply amplifying and decaying, but they

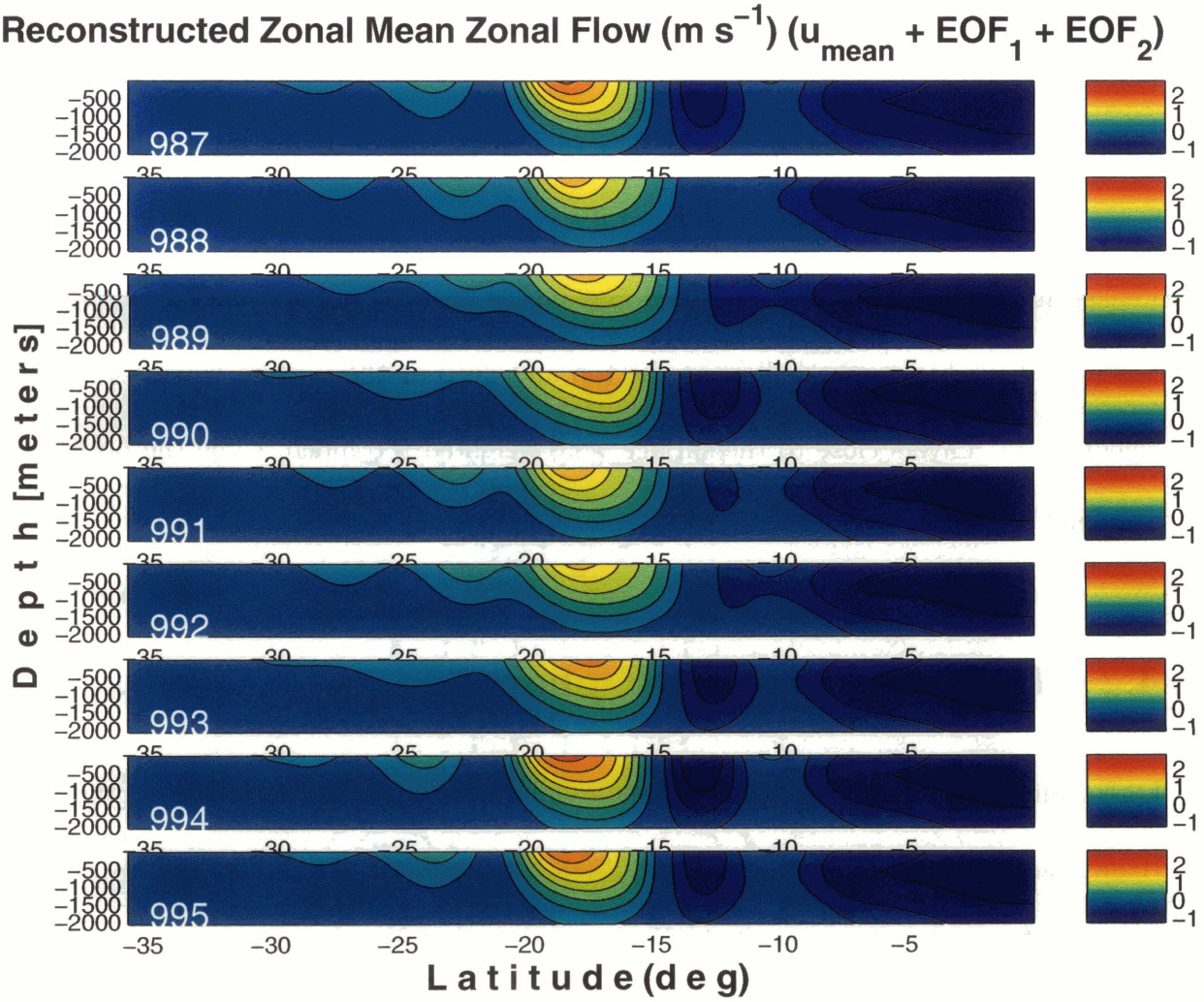

Figure 4.4: Time series of the reconstructed zonal flow using the leading two modes ($u_{recon} = u_{mean} + PC1 \cdot EOF_1 + PC2 \cdot EOF_2$).

are also migrating. Thus, the second EOF allows us to capture the evolution of the secondary jets shown in Figure 4.4.

Therefore, in order to succinctly describe the dynamics involved, all we need are the two EOFs since it describes the zonal flow as either increasing or decreasing and as being displaced equatorward or poleward at any given time. Mathematically, the leading two principal components capture these characteristics. When the jet moves poleward (equatorward), PC1 will be positive (negative) and similarly when the zonal flow is anomalously large (weak), PC2 will be positive (negative). Therefore, we define Phase A as PC1<0 and PC2<0, Phase B as PC1<0, PC2>0 and so forth. A complete summary of the mathematical and physical representation can be seen in Table 1.

The purpose of classifying each year with a particular phase allows us to perform many tasks. Firstly, we have now succinctly categorized the variability into just four bins as described in Table 1. Secondly, since there is a lot of interest in how the zonal index fluctuates from an equatorward to a poleward displacement of the jet (e.g. Yu and Hartmann 1993; Feldstein and Lee 1996) by categorizing each year into four phases, conditions for the onset of a particular zonal index can be analyzed. In particular, EOF phases will be used for diagnostic plots. This is done by compiling the years associated with each phase, then performing an average of that phase for that diagnostic. As we have seen in section 3, had we done a time-average of the entire period, the migrating jets would not be seen. Thus, the primary reason for utilizing EOF phases allows secondary jets to be preserved and analyzed. A visual representation of the zonal flow can be seen in Figure 5.1 with each phase

corresponding to the previous description shown in Table 1.

Using PC1 and PC2, we classify every year to one of the above four phases. For example, a sixty-year time series is shown in Figure 4.5. In general, the zonal flow changes adhere to the following sequence: Phase A $\rightarrow$ Phase B $\rightarrow$ Phase C $\rightarrow$ Phase D and then repeats back to A. This sequence is dictated by the behavior of the secondary jets. Since they migrate equatorward, the principal components (PC) of both modes need to change sign to allow the secondary jets to advance equatorward leading to the systematic clockwise progression through each EOF phase as shown in Fig 4.5.

If this sequence were to be followed strictly, during the onset of a low zonal index, these two modes imply negative zonal flow anomalies at the location of the primary jet. Alternatively, there is typically positive zonal flow anomalies at the jet during the transition to a high zonal index. Each part of the sequence is followed by the correct phase at least *sixty*-four percent of the time, e.g. the conditions prior to the onset of Phase A were correctly observed to be in Phase D sixty-four percent of the time and incorrectly by Phase B or C thirty-six percent of the time. The conditions prior to Phase B were observed to be in Phase A eighty-five percent of the time. The complete statistical results describing the conditions prior to the onset of each phase and zonal index is given in Table 2.

These results show that a significant percentage of the time (seventy-four percent) positive zonal flow anomalies were coincident with jet prior to an equatorward displacement, i.e. the conditions prior to the onset for a high index are described by Phase B. Alternatively, only sixty-one percent of the time, the jet was in Phase D prior to a negative zonal index. This

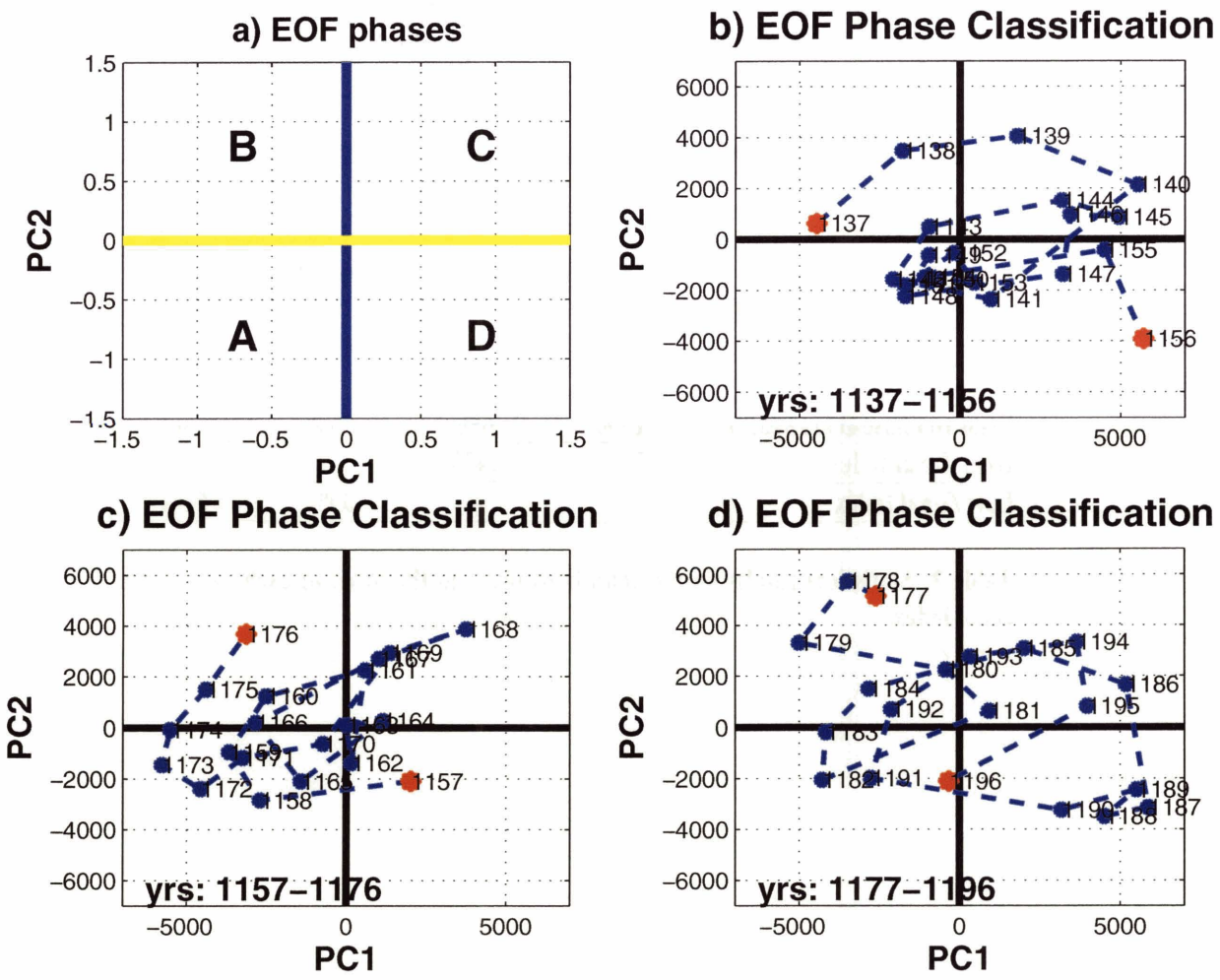

Figure 4.5: (a) Graphical display of the EOF phases. Note the abscissa is PC1 and the ordinate is PC2. (b), (c) and (d) A time series of the jet characteristics as described by the EOF phases.

shows that the sequence is not symmetric, e.g. there is a stronger relation between Phase A and Phase B than there is between Phase D and Phase A.

	Phase A	Phase B	Phase C	Phase D
Displacement	Equatorward	Equatorward	Poleward	Poleward
Strength	Decreasing	Increasing	Increasing	Decreasing
PC1	Negative	Negative	Positive	Positive
PC2	Negative	Positive	Positive	Negative

Table 1: Physical characteristics of the four phases defined through the first two EOFs.

	Phase A	Phase B	Phase C	Phase D
Prior to Phase A (95 years)	–	7%	29%	64%
Prior to Phase B (71 years)	85%	–	15%	0%
Prior to Phase C (75 years)	16%	79%	–	5%
Prior to Phase D (72 years)	19%	6%	75%	–
High Zonal Index	26%	74%	–	–
Low Zonal Index	–	–	39%	61%

Table 2: Statistical results on the conditions prior to the onset of each phase and zonal index.

Chapter 5

Eddy Properties

5.1 Eddy-Mean Flow Interaction

Despite the presence of bottom drag, zonal flow anomalies (Figure 4.1) are observed to persist for relatively long time scales, an indication that anomalies must be maintained by some forcing. The forcing likely responsible arises through eddy-mean flow interaction. There are two ways for eddies to interact with the mean flow: (1) through the divergence of the eddy momentum fluxes and (2) through the divergence of the eddy heat fluxes. To show this, we start from the momentum equation in Cartesian coordinates:

$$\frac{d\vec{u}}{dt} + f\hat{z} \times \vec{u} = \frac{-1}{\rho}\nabla P - g\hat{z} + \frac{\partial \tau}{\partial z} \tag{5.1}$$

where f is the Coriolis parameter, $\vec{u}$ is the velocity vector, ρ is the density, g is gravity and τ is the dissipation owing to friction. Taking the zonal average, linearizing from a basic

time-mean state, and written in spherical coordinates, the zonal component of equation 5.1 is as follows:

$$\frac{\partial[u]}{\partial t} - f[v] = -\frac{\partial[u'v']\cos^2\phi}{a\cos^2\phi\partial\phi} + \frac{\partial\tau}{\partial z} \tag{5.2}$$

where square brackets indicate a zonal average, $u' = u - \bar{u}$, $\bar{u}$ is the time-averaged flow, v is the meridional velocity, a is the earth's radius, and ϕ is the latitude. In the following discussions, the first term on the right-hand side (RHS) will be referred to as the eddy forcing term. Equation 5.2 shows that the flow tendency is part of a four-way balance with the Coriolis force, the eddy momentum flux, and friction.

However, it can be shown that the heat forcing can be just as important as the eddy momentum forcing in driving the zonal mean circulation through eddy heat fluxes and adiabatic motion. The thermodynamic equation shown below can be manipulated to unite the two forcings.

$$\frac{D\theta}{Dt} + \sigma w = \frac{Q}{c_p} \tag{5.3}$$

Taking the zonal average, linearizing from a basic mean state, retaining terms to that are of order Rossby or higher, and converting into spherical-height coordinates, we obtain:

$$\frac{\partial T}{\partial t} + \frac{N^2 H}{R}[w] = [Q] - \frac{\partial[v'T']\cos\phi}{a\cos\phi\partial\phi} \tag{5.4}$$

where N is the Brunt-Väisälä frequency, Q represents diabatic effects such as radiation and

latent heat release, R is the ideal gas constant, and H is the scale height.

This shows the vertical velocity is influenced by the convergence of the eddy heat flux. Therefore, following Edmon et al. (1980), we redefine the vertical velocity to represent only the diabatic motions and remove the eddy heat flux dependence by introducing the residual mean velocities:

$$\widetilde{w}^* = w + \frac{R}{H}\frac{\partial}{a\cos\phi\partial\phi}\frac{[v'T']}{T_z} \tag{5.5}$$

$$\widetilde{v}^* = v - \frac{R}{H}\frac{\partial}{\partial z}\frac{[v'T']}{T_z} \tag{5.6}$$

The meridional component, $\widetilde{v}^*$, represents the meridional motion necessary to conserve mass in the residual mean meridional circulation, and the vertical component, $\widetilde{w}^*$, represents the vertical velocity without the contribution of the eddy heat flux. If we now substitute equation 5.5 into equation 5.1 we obtain the transformed Eulerian mean flow interaction.

$$\frac{\partial[u]}{\partial t} - f[\widetilde{v}^*] = \nabla\cdot\vec{F} + D \tag{5.7}$$

where

$$\vec{F} = \Big(- a\cos\phi[u'v'], a\cos\phi f\frac{[v'T']}{[T_z]}\Big) \tag{5.8}$$

We refer to $\vec{F}$ as the Eliassen-Palm (EP) flux vector. The divergence of the EP flux, or more specifically, the combination of both the divergence of the eddy momentum flux and the eddy heat flux, shown in equation 5.7 5.8, act in concert to alter the zonal-mean zonal flow.

An added benefit in analyzing plots of the EP flux offer a visual representation of wave motions. For example, let

$$\psi' = a(y,z,t) \cdot cos(kx + ly + mz - \omega t) \tag{5.9}$$

where a is a slowly varying function of latitude, height and time. Using quasi-geostrophic approximations, it can be shown (e.g. Andrews et al. 1987)

$$\vec{F} = (\hat{j}C_{gy} + \hat{k}C_{gz}) \cdot A \tag{5.10}$$

where

$$C_{gy} = \frac{2kl[q_{py}]}{(k^2 + l^2 + m^2/S)^2} \tag{5.11}$$

$$C_{gz} = \frac{2km/S[q_{py}]}{(k^2 + l^2 + m^2/S)^2} \tag{5.12}$$

$$A = \frac{\rho}{2}[q'^2](\frac{\partial q}{\partial y})^{-1} \tag{5.13}$$

are the meridional and vertical group velocity for Rossby waves respectively, A is referred to as the wave activity, S is the stratification parameter and $[q_{py}]$ is the zonally- and time-averaged quasi-geostrophic potential vorticity meridional gradient.

If $A > 0$, then Equation 5.10 shows that to a rough approximation

$$-[u'v'] \sim C_{gy}. \tag{5.14}$$

Therefore, if we assume that $[q_{py}]$ is dominated by β then A will be positive and 5.14 holds.

Since values of β increase equatorward, then the group velocity, and thus the horizontal EP flux will have latitudinal asymmetry. In particular, there will be a bias to have larger values on the equatorward side than the poleward side of the source of the eddy activity.

Finally in this section, it may be worthwhile to give some comments about the residual circulation. From equation 5.7, not only do the effects of the divergence of the Eliassen-Palm flux alter the zonal-mean circulation, but also the residual meridional circulation. Recall in equation 5.5, the purpose of solving for the time-mean residual circulation is to eliminate the adiabatic effects and focus on the diabatic effects. In the interior of our domain, with no friction nor diabatic heating, the residual circulation winds up being virtually zero and we can conclude that effects from the residual circulation will not play an important role in this system and hence, will not be discussed further. Therefore, we focus our attention in the next couple of sections on the terms on the right hand side of 5.7 – the Eliassen-Palm fluxes and the role of friction in order to describe the migrating jets.

5.2 Eddy Effects

The arrows in Figure 5.1 represent the wave activity associated with the total EP flux in relation to each phase as described in section 4.2. In all cases, most of the eddy activity is poleward of 12°S. There is almost no eddy activity near the equator because of the model-imposed forcings at this region. As discussed in section 3, this region is highly stable, and thus, it comes as no surprise baroclinic waves are not generated.

In all EOF phases, upward wave activity is observed, with the strongest activity near the

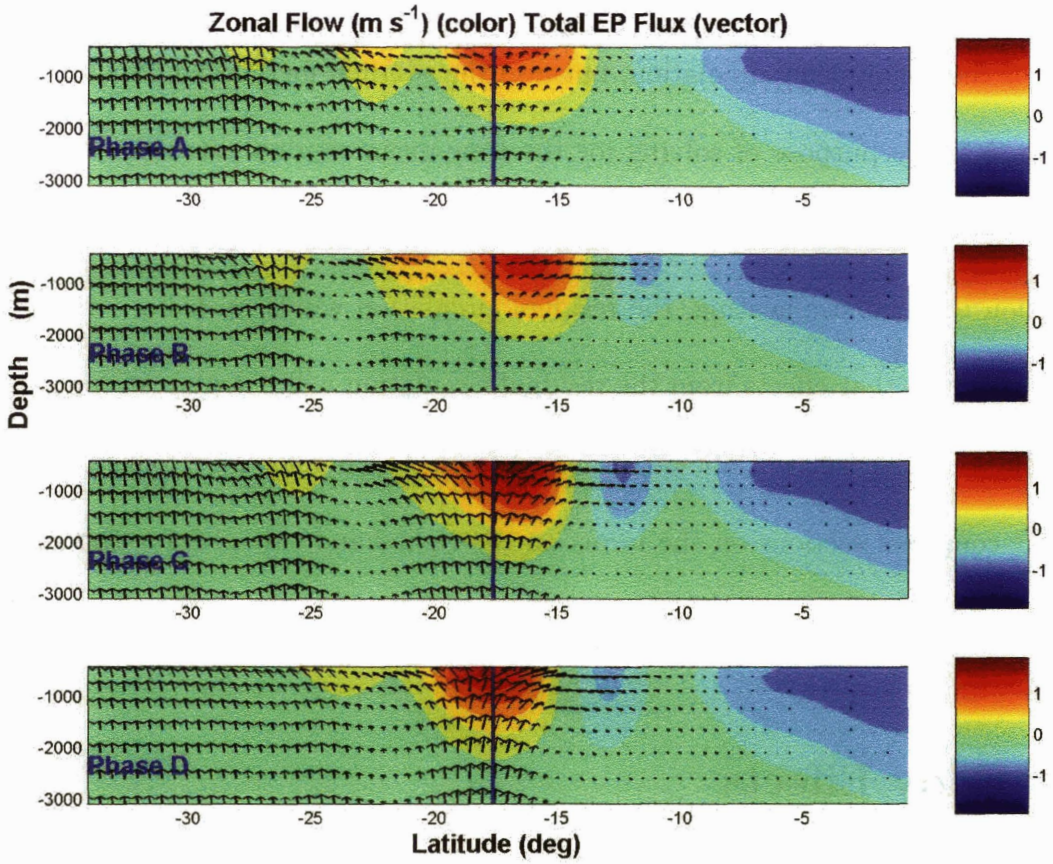

Figure 5.1: Eliassen-Palm cross sections. The total EP flux vectors for each EOF phase (labelled on bottom left corner) are plotted over zonally-averaged zonal flow.

jet in Phase D and the weakest in Phase B. As described in equation 5.14, the horizontal eddy momentum flux is in the opposite direction as the horizontal EP flux. Using equation 5.9, a similar procedure could be done to show that the vertical eddy momentum flux $[u'w']$ is in the opposite direction of the vertical EP flux. With the EP flux directed upward in all phases, it comes with little surprise that this implies that (eastward) momentum is being transferred downward. Furthermore, focusing on the horizontal EP flux, poleward of the primary jet (indicated by the white line in Figure 5.1), eastward momentum is being transferred equatorward, while north of 17°S, momentum is being redistributed toward the jet. Not surprisingly, a time-averaged plot of the effect of eddies is to bring positive momentum both downward and toward the jet.

Comparing the different phases, both the eddy heat flux and eddy momentum flux are more dominant in the high zonal index (Phase C and D) than in the low zonal index (Phase A and B). Also, there is only a marginal difference in wave activity between the two high index phases (Phase C and Phase D) and similarly for the low index phases (Phase A and Phase B) when especially comparing the separate two zonal indexes.

The horizontal and vertical component of the EP flux vectors indicate different effects on the primary zonal jet. The vertical component reduces the vertical shear, while the horizontal component acts to increase the horizontal shear. Causality cannot be determined here, but there is a high correlation between the two components of the EP flux. Comparing the low and high zonal index near the primary jet, whenever stronger horizontal momentum gets deposited into the primary jet, the values for the downward vertical momentum flux are

anomalously large values. Alternatively, weak downward vertical momentum flux is observed whenever the horizontal eddy momentum fluxes were anomalously weak.

We speculate that the EP fluxes shown are just a consequence of the system being inherently baroclinically unstable. Due to this instability, eddy heat fluxes are generated and act to reduce the vertical shear by bringing positive momentum fluxes downward. Concurrently, since the energy cascades to the Rhines scale, which happens to be larger than the Rossby radius of deformation, then as shown by Held and Andrews (1980), the sign of the vertically-integrated eddy momentum flux must be directed into the jet. When the jet is anomalously strong, its baroclinicity increases and the instability acts to decrease the vertical shear more vigorously.

Poleward of 30°S, the main jet shows a substantial amount of upward wave activity propagation. We note that the static stability is low. But in any case, since the vertical temperature gradient was close to zero poleward of 30°S and is in the denominator of $F_{(z)}$, this results in a large vertical EP flux.

We will sidestep this issue by focusing on the anomalous EP flux vectors shown in Figure 5.2. In this figure, anomalous baroclinic activity can be inferred by looking at the contoured zonal flow anomalies. Areas of anomalously positive zonal flow can be equated to a positive deviation of the vertical shear. Because the Eady growth rate is proportional to the vertical shear, this leads to anomalous baroclinic wave activity (Eady 1949). As these waves propagate away from this region, momentum gets transported towards the source of wave activity.

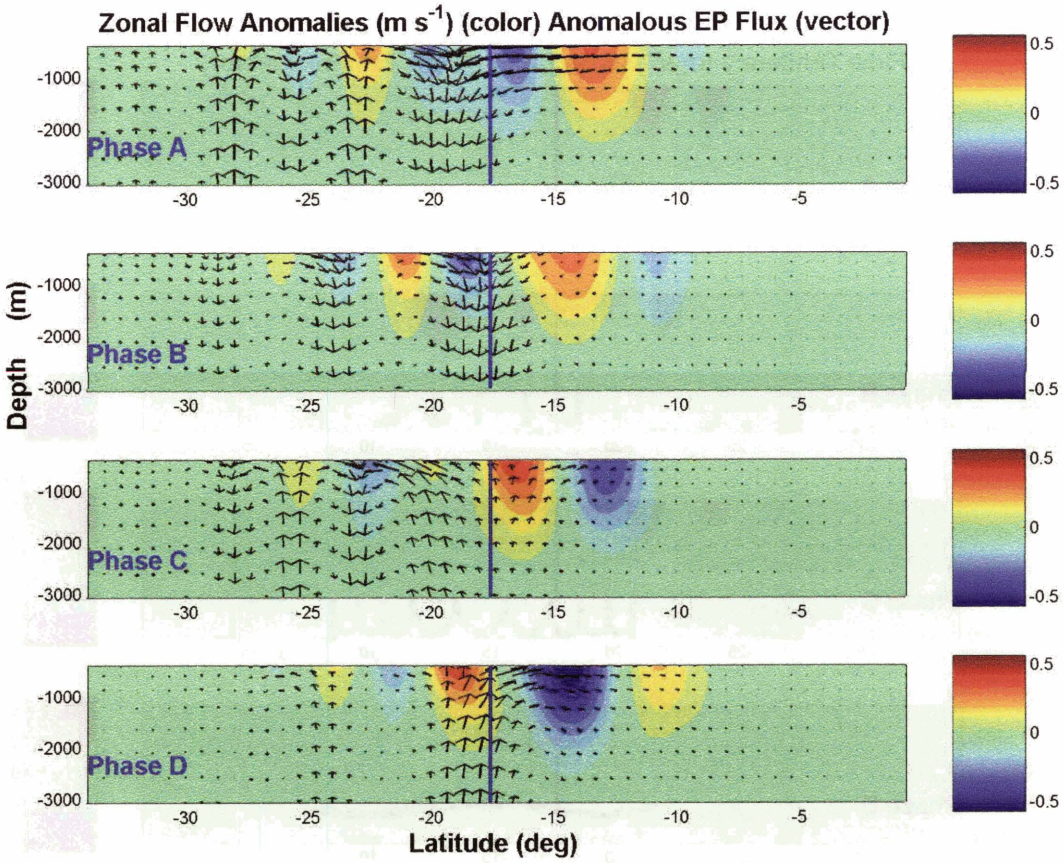

Figure 5.2: Anomalous Eliassen-Palm cross sections. Anomalous EP flux vectors for each EOF phase are plotted over the zonally-averaged zonal flow anomalies. Each phase is labelled at the bottom left corner of plot.

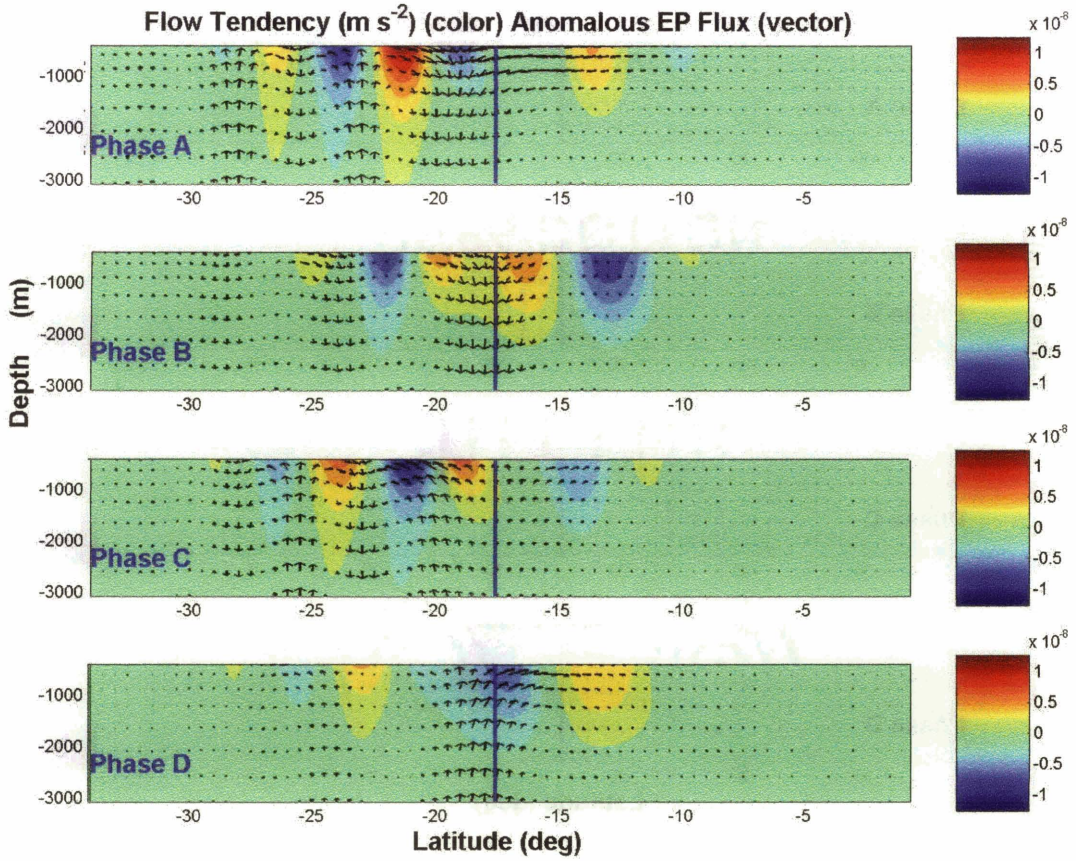

Figure 5.3: Same as Fig. 5.2 but with the flow tendency contoured instead.

From equation 5.7, assuming no friction, the divergence of the EP flux should lead to an acceleration of the mean flow. Figure 5.3 shows that the divergence is not aligned with the flow tendency. In fact, upon a closer inspection of the divergence of $\vec{F}$ and Figure 5.3 shows that they are not synchronized in time or in space and this implies frictional forces cannot be neglected. We will soon show that in the presence of moderate friction, divergence of the EP flux will be associated with positive flow anomalies and not with a positive flow tendency. (This will be discussed in greater detail in section 6.1.)

In any case, the zonal flow anomalies (overlayed in Figure 5.2) are maintained by baroclinic instability processes. Positive (negative) zonal flow anomalies are generated and maintained in regions where prior conditions demonstrated anomalously weak (strong) baroclinicity.

5.3 Momentum Budget

As discussed in the previous section, friction cannot be ignored. Here in this section, we will take a closer look at the frictional effects in the context of the momentum budget. Since the jets are equivalent barotropic, and we are more interested in how momentum gets redistributed latitudinally, we proceed by integrating equation 5.7 across the entire depth, the vertical component of the EP flux must vanish, leaving only the horizontal component of the EP flux and friction:

$$\frac{\partial < [u] >}{\partial t} = -\left\langle \frac{\partial [u'v'] \cos^2 \phi}{a^2 \cos^2 \phi \partial \phi} \right\rangle + \tau_{surf} - \tau_{bot} \tag{5.15}$$

where vertically-integrated values are represented by angle brackets. The first term on the RHS will be called the eddy forcing.

Equation 5.15 demonstrates that the vertically-integrated flow tendency is balanced by the vertically-integrated eddy forcing and the frictional effects. Note the Coriolis term must vanish owing to the zonally-averaged mass conservation.

A time-average of equation 5.15 is shown in Figure 5.4a. When time-averaging, the flow tendency averages to zero and the only terms that contribute are on the RHS. To a first-order approximation, the wind stress is inputting momentum into the fluid and being removed by the bottom drag.

Forcing provided by the divergence of the horizontal EP flux peaks between 20°S and 15°S providing evidence that the observed jet in this region is indeed eddy-driven. Physically, through the wind stress, momentum is being transferred into the ocean primarily between 40°S to 30°S. Then from figure 5.4, the eddy momentum flux is directed equatorward from 50°S to 17°S and converges at the jet. However, this forcing is counteracted by the bottom drag.

By performing a time-average of equation 5.15 information cannot be gathered for anomalous activity such as the flow tendency. In Figure 5.5, we remove the time-average stipulation, and analyze the annually averaged anomalous terms of the vertically-integrated momentum equation for particular years. Since the wind stress applied to the top layer is constant in time, this term cannot be associated with any *anomalous* activity.

The flow tendency is not balanced by just the eddy forcing; instead, it is the combination

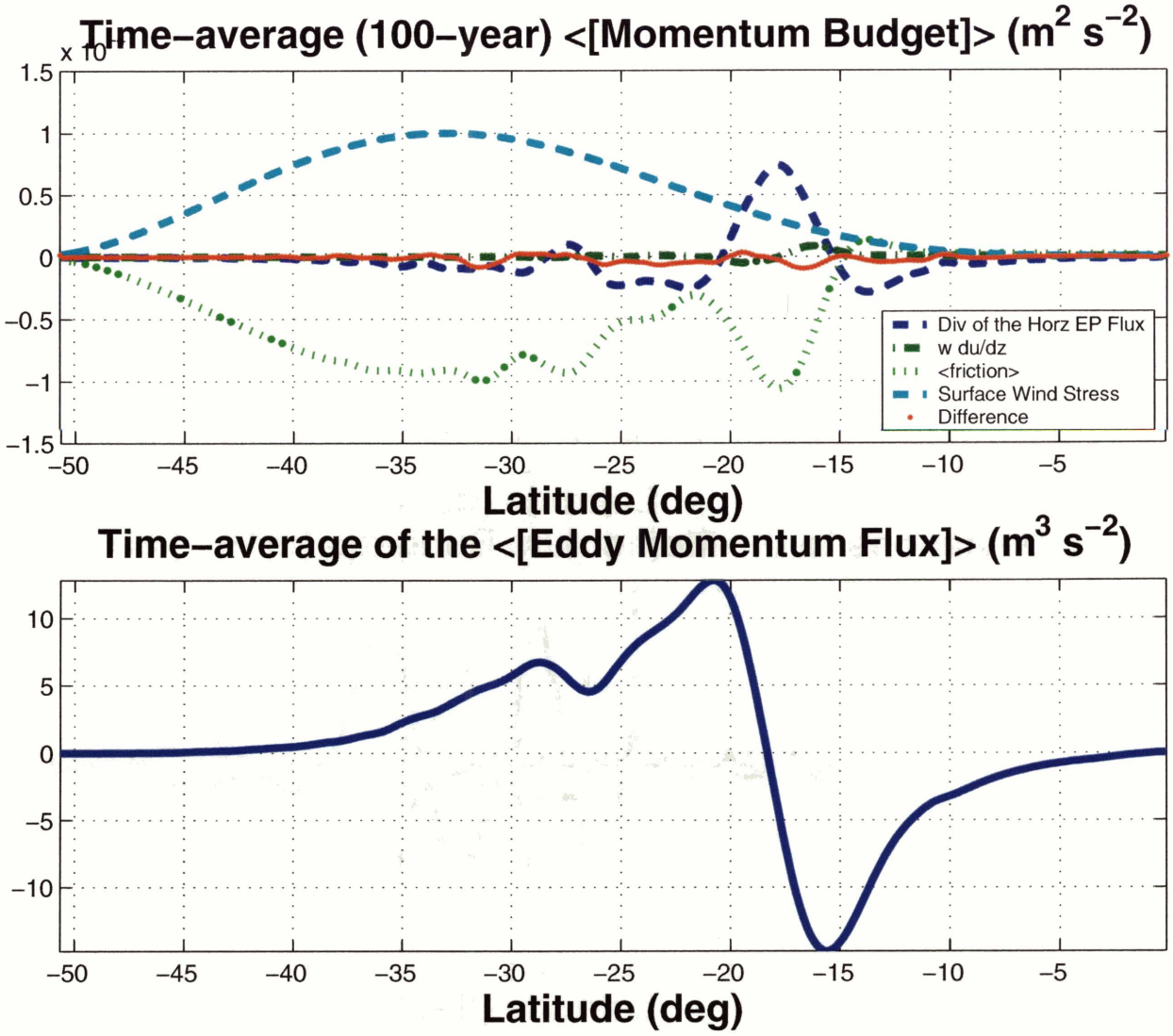

Figure 5.4: (a) Time-averaged quantities of the vertically-integrated zonal momentum budget. (b) Time-average of the vertically-integrated eddy momentum flux $< [u'v'] >$.

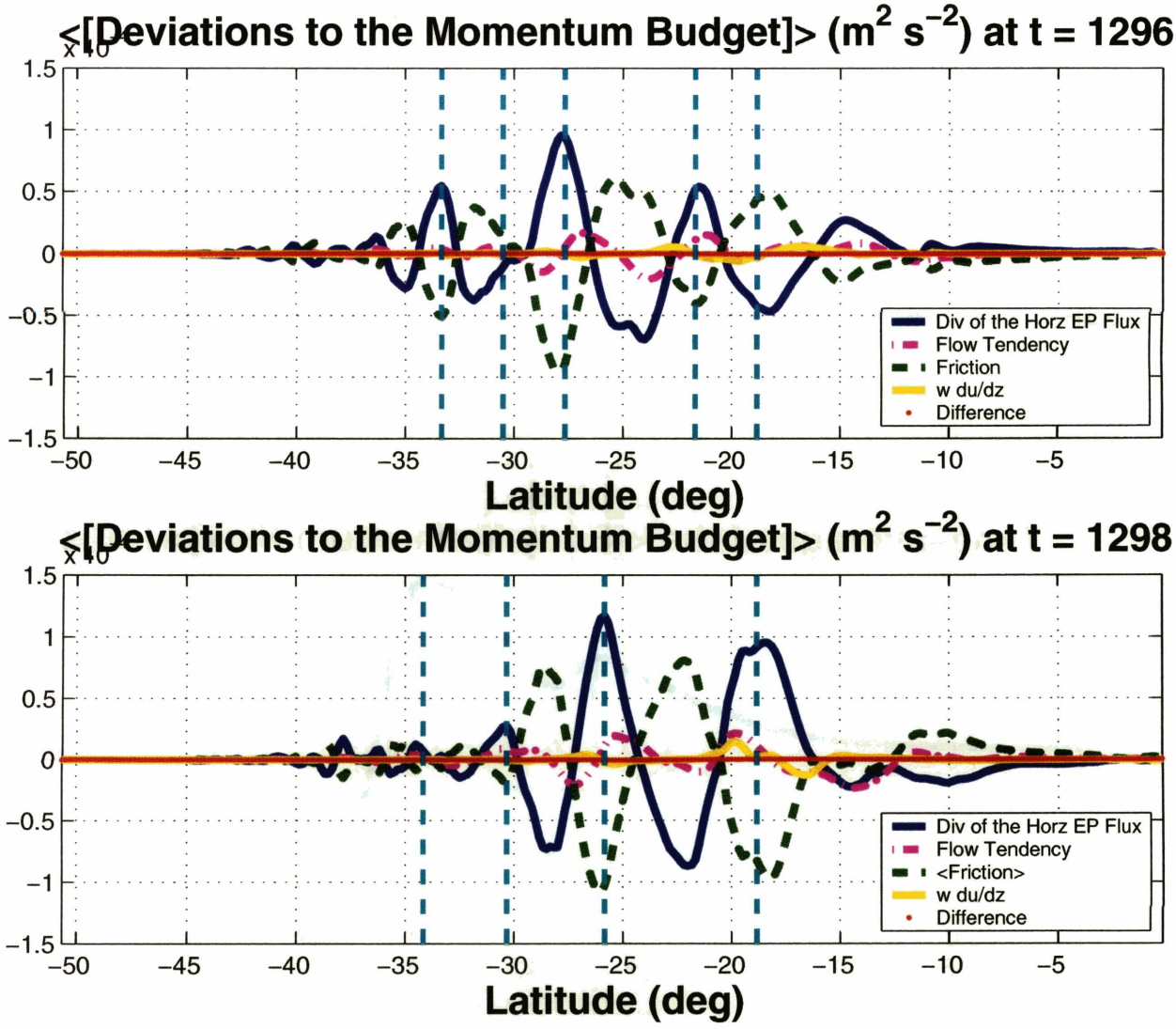

Figure 5.5: Terms to the vertically-integrated zonal momentum balance for (a) year 1296 and (b) year 1298. Vertically dashed lines correspond to maximum zonal flow anomalies.

of eddy forcing and the friction that balances the $\frac{\partial[u]}{\partial t}$ term. The friction is the same order of magnitude as the eddy forcing, and the flow tendency is only about one-tenth of the forcing. This shows this regime is in a quasi-steady balance between the eddy forcing and friction, and the flow tendency is essentially a residual in equation 5.15.

Chapter 6

Comparison to Simple Models

6.1 Frictional Effects

Before continuing on the results of the MITGCM, we employ a simple model because results can be more meaningful and straightforward. This can also be used as a good check and balance between the two models. The purpose of this simple model is to prescribe a forcing and understand how the flow changes with varying frictional values. As we shall soon see, friction not only impacts the flow strength, but also the flow's phase relationship with the forcing.

The simple model solves a simpler form of equation 5.15, as given below:

$$\frac{\partial < [u(t)] >}{\partial t} = F(t) + D(t) \tag{6.1}$$

where F represents the anomalous eddy forcing and D represents the anomalous bottom

drag.

A time series of the MITGCM shows the anomalous eddy forcing exhibits a sinusoidal behavior. Hence, for this simple model, we represent F as the following:

$$F(t) = sin(\omega t) \tag{6.2}$$

To get an expression for D, we refer to equation 2.1, which defines how the MITGCM calculates the bottom drag. If we linearize equation 2.1, the anomalous bottom drag will be a function of both the eddy kinetic energy and the anomalous zonal flow at the lowest layer. If we make the assumption that the anomalous KE term is only a function of the zonal flow, then D depends on both u'_{bot} and u'. Furthermore, if we assume the perturbations to u'_{bot} are much smaller than to u', then D only depends on u', which is directly proportional to the vertically-integrated zonal flow because of the equivalent barotropic structure. Therefore, we can obtain a simple linear parametrization of the anomalous bottom drag:

$$D = C_D \times < [u'] > \tag{6.3}$$

where C_D is the drag coefficient and $< [u'] >$ represents the anomalous vertically-integrated zonally-averaged zonal flow.

Now that there are expressions for both F and D, we substitute them into equation 6.1 to obtain:

$$\frac{\partial < [u(t)] >}{\partial t} - C_D \cdot U(t) = sin(\omega t) \tag{6.4}$$

This leads to the following analytical solution for the zonal flow:

$$< [u(t)] >= Imag(\frac{e^{i\omega t}}{i\omega - C_D}) \tag{6.5}$$

Therefore, $< [u] >$ depends only on the drag coefficient and the frequency of the forcing. Also, the above equation shows that as C_D approaches zero, the zonal flow will be ninety-degrees out of phase with the forcing; meanwhile, as C_D approaches infinity, $< [u] >$ will be in phase with the forcing.

For this model, since we are interested in the frictional effects, we vary C_D, but set $\omega = 1$ for all runs. Graphical solutions are shown in Figure 6.1. In the inviscid case, clearly the flow tendency is solely balanced by the eddy forcing, and thus is in phase with F. Because the flow tendency and the flow itself must be in quadrature, the zonal flow is out of phase with the forcing.

When increasing the drag coefficient slightly, the $\frac{\partial u}{\partial t}$ must balance with both the eddy forcing and friction. This damping obviously lowers the flow's magnitude, but will always be in phase with the flow. The second plot contains an incremental increase in the drag coefficient. The flow tendency must balance both the friction and the forcing. Because frictional forces are strongest when the flow speed is maximum and weakest when the flow speed is zero, the phase of the zonal flow shifts in the direction of the forcing. In essence, friction counteracts the forcing resulting in a weaker flow tendency and causing the flow tendency to be out of phase with the forcing.

The third run uses a drag coefficient ten times larger than the previous run. This will

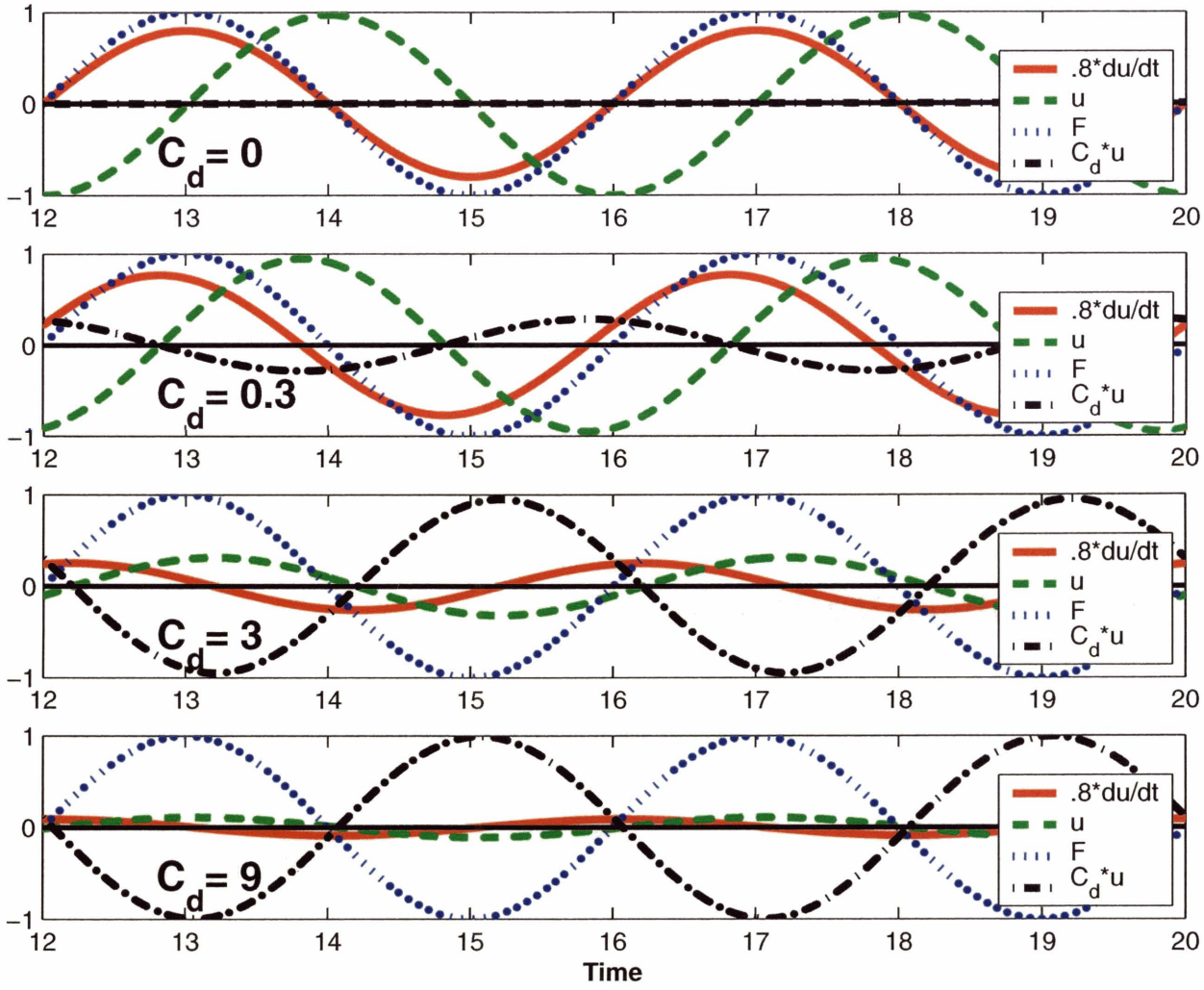

Figure 6.1: Simple model of flow tendency balancing both the eddy and frictional forces for (a) the inviscid case with $C_D = 0$, (b) "slight friction case" with $C_D = 0.3$, (c) "moderate friction case" with $C_D = 3.0$ and (d) "extreme friction case" with $C_D = 9.0$.

be referred to as the "moderate friction case" where the friction and the forcing are of the same order of magnitude. Both the flow tendency and the zonal flow have been reduced by a factor of two and have been phase shifted such that the zonal flow is almost in phase with the forcing. Since the flow tendency only changes the zonal flow anomalies, when friction is sufficiently large, which is the case for this run, the forcing no longer has the highest correlation with the flow tendency, but instead with the zonal flow anomalies.

Finally, when friction is extremely strong, the bottom plot shows the forcing and the friction nearly cancelling one another. Since the flow is in phase with the friction, this implies that the flow is also in phase with the forcing and the flow tendency is now in quadrature with the forcing, consistent with the results of our analytical solution.

6.2 Sphericity Effects

Under symmetric circular atmospheric jets on a sphere, waves have been shown to break outward i.e. equatorward (Nakamura and Plumb 1994). Observations of the Eliassen-Palm flux in the observed atmosphere indicate that Rossby waves generally propagate equatorward (Edmon et al. 1980).

From Chen and Robinson (1992), the refractive index is as follows:

$$n^2 = \frac{\partial q}{\partial \phi}\frac{1}{[u] - (a\sigma cos\phi)/s} - \frac{s^2}{a^2 cos^2\phi} - \frac{f^2}{4N^2H^2} \tag{6.6}$$

where a is the earth's radius, N^2 is the buoyancy frequency, σ is the wave frequency, q is the potential vorticity, and s is the spherical zonal wave number.

From equation 6.6, we can show why Rossby waves have this greater tendency to propagate equatorward. In regions of wave propagation, from WKB theory, waves are refracted toward larger n^2. Therefore, due the two terms on the RHS of equation 6.6, the index of refraction values increases equatorward. These spherical terms are what causes Rossby waves to propagate more equatorward, and hence, there will be a latitudinal bias in the refractive properties of the Rossby waves.

Using another simple model (Figure 6.2) a demonstration on the implication of an equatorward bias in wave propagation is shown. The first run shows a symmetric wave propagation at y = 0. This causes a peak eddy momentum flux convergence at y = 0. In the second run, we keep the non-divergent eddy activity at y = 0, but slightly increase the equatorward propagation and slightly decrease the poleward propagation. Although the amplitude of the maximum convergence remains the same, it comes as no surprise, an equatorward bias in the eddy forcing has developed. Therefore, since the convergence of eddy momentum flux occurs on the equatorward flank of the jets, equatorward migration occurs.

6.3 Sphericity and Frictional Effects

In this final exercise, we combine the effects discussed in the two previous sections and examine how they impact the spatial and temporal evolution of the zonal flow. Integrating equation 6.1 again, but this time, we set the initial flow to have a sinusoidal one-dimensional spatial structure:

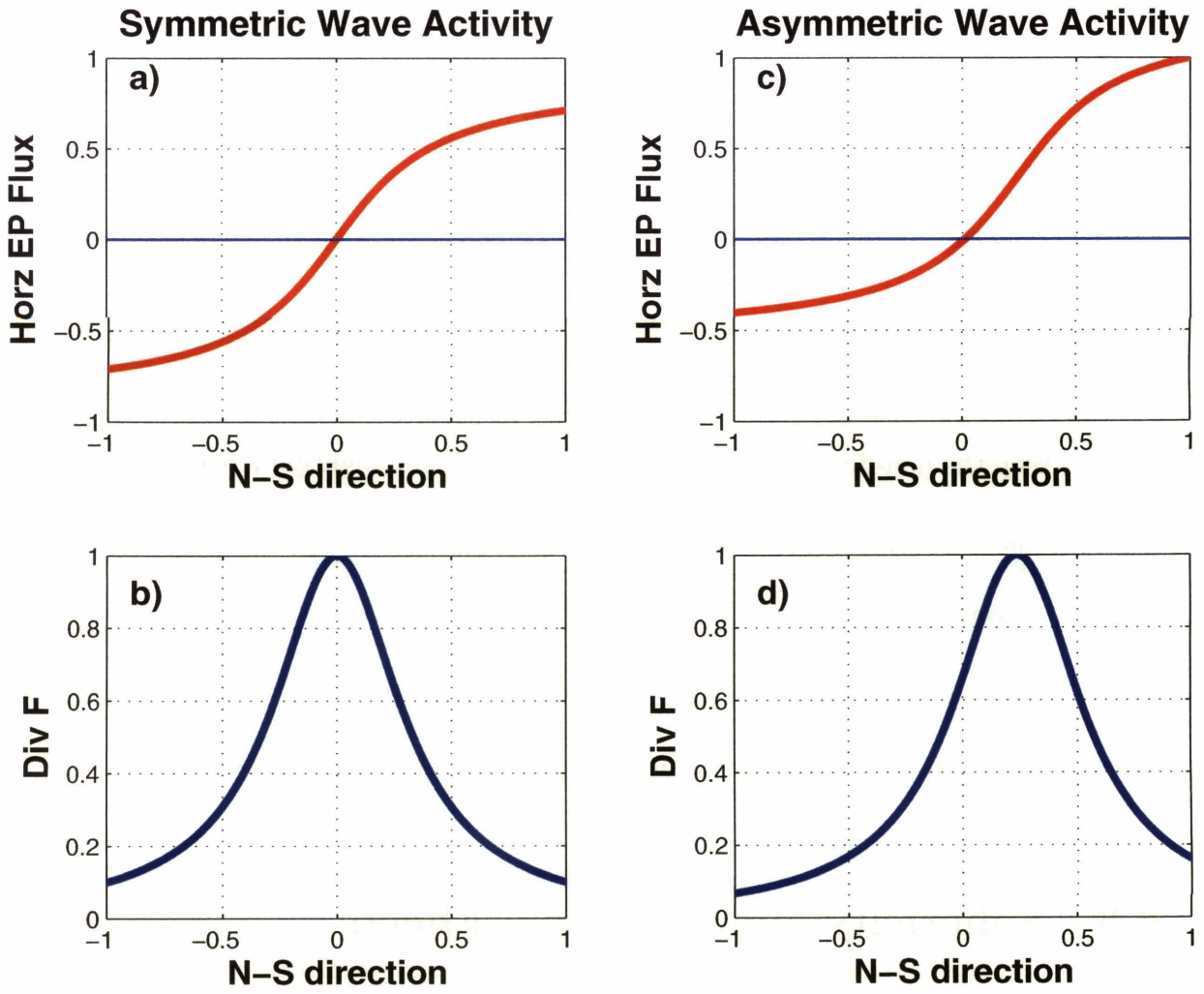

Figure 6.2: Simple model with (a) symmetric wave activity, (b) symmetric eddy forcing, (c) asymmetric wave activity with an equatorward bias and (d) asymmetric eddy forcing with an equatorward bias.

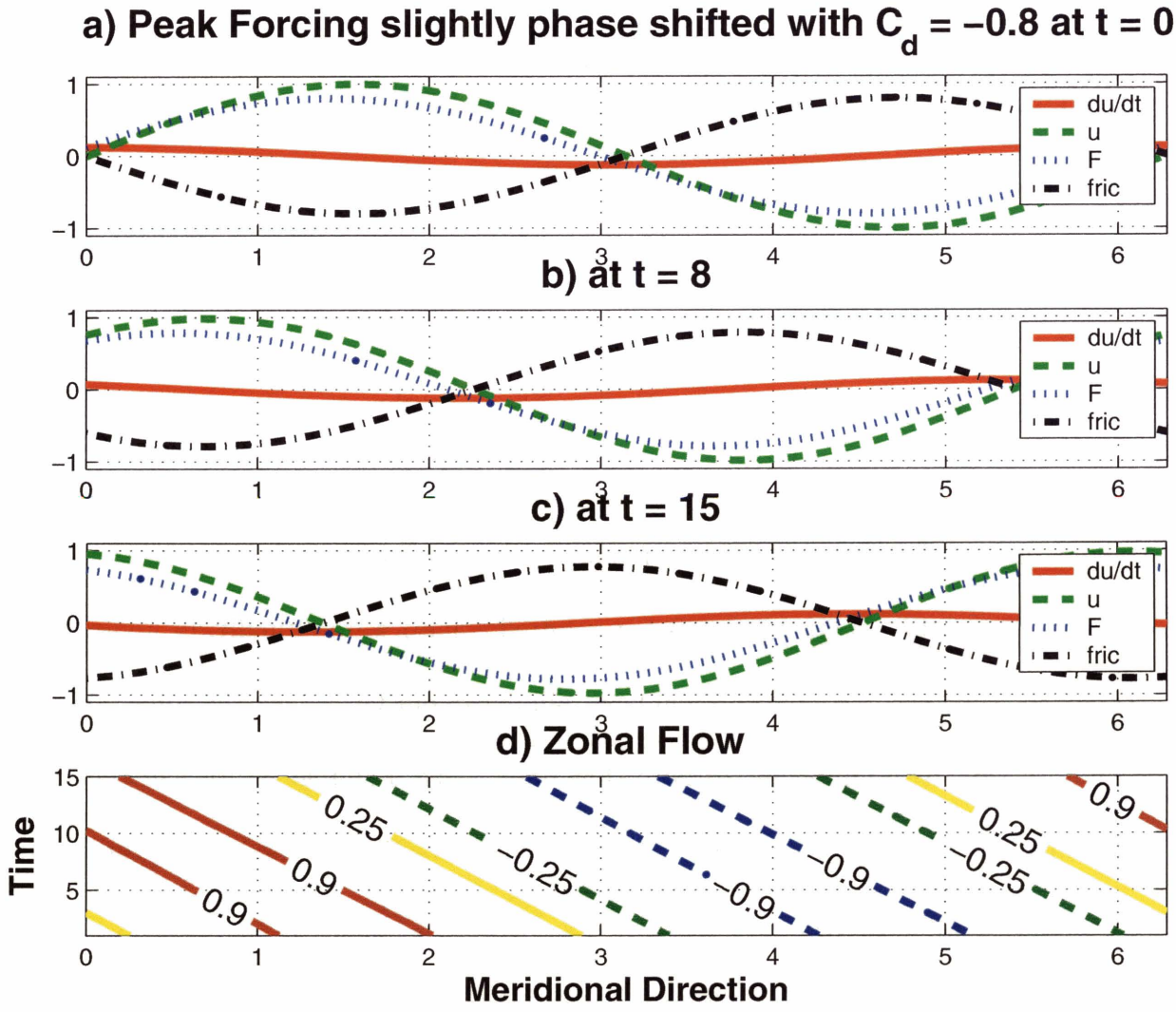

Figure 6.3: Simple model combining the effects of friction and sphericity. The meridional value of zero has been arbitrarily been defined as the equator. For all time steps, the maximum forcing is prescribed to have the same spatial relationship as the zonal flow, but shifted slightly equatorward. The top three plots show the flow tendency, the zonal flow, the eddy forcing and friction at the particular time frame. The bottom plot indicates the zonal flow as a function of space and time.

$$u(y,0) = sin(y) \tag{6.7}$$

The forcing here is prescribed to have the same spatial relationship as the zonal flow, but shifted slightly equatorward. This can be justified by the model results of the MITGCM (see Figure 5.2) and from section 6.2. We also parameterize friction as a linear function of the velocity, which was previously done in section 6.1 and set the drag coefficient, C_D, equal to 0.8.

Figure 6.3a shows the initial conditions. The zonal flow is as described in equation 6.7, and the forcing has been shifted slightly equatorward. The maximum flow tendency occurs where the zonal flow is near zero, similar to the results found in section 6.1. In Figure 6.3b and 6.3c, the maximum speeds have shifted equatorward. Finally, in Figure 6.3d, this shows the time-evolution of the zonal flow. Similar to our GCM run, the zonal flows migrate equatorward. It is important to note that under such a simple setup, had there been no bias in the forcing, the frictional effects would have exactly cancelled the forcing preventing anomalies to ever emerge.

Varying the frictional parameter, C_D can also lead to changes in how fast the jets migrate. Increasing the friction but keeping the forcing the same, flow anomalies eventually get dissipated. But before they do so, the migration took longer for the jet to reach the same point. This proves that not only is the forcing asymmetry important, but also the amount of frictional forces is key in understanding how jets migrate.

Chapter 7

Discussion

7.1 Migrating Jets

Comparing the GCM and the simple model, discussed in section 6.1, the GCM results best matches with the "moderate friction case." The anomalous eddy forcing has a higher correlation with the zonal flow anomalies than the flow tendency. The forcing is approximately in phase with the frictional force, and the flow tendency is about one-tenth of the forcing as shown in Figure 5.5. These are all indications that there is "moderate friction" involved.

Assume a symmetric zonal jet with a similarly symmetric eddy forcing. At the location of the jet maximum, friction is greatest and counteracts the eddy forcing. However, as discussed in the previous section, away from the jet where the zonal flow anomalies are at a minimum, friction will be small, thus allowing the forcing to accelerate the mean flow. This method explains the *means* in how zonal flow anomalies could migrate, but doesn't explain the *cause* for such a migration.

Referring back to Figure 5.2, the spherical effects described in section 6.2, can be observed. In regions of positive zonal flow anomalies, horizontal EP flux is stronger on the equatorward flank of the secondary jets. In Figure 7.1, snapshots of the zonal flow anomalies and the anomalous horizontal EP flux are shown. It is clear between 35°S and 20°S, there is an asymmetry associated with the eddy momentum flux with respect to the zonal flow anomalies. In each time frame, anomalous $-[u'v']$ is stronger on the equatorward flank of the secondary jets than its poleward counterpart.

Going back to Figure 5.2, both the vertical and horizontal EP fluxes are plotted. However, since the eddy heat flux ultimately redistributes momentum vertically, we are only interested in the horizontal component when investigating the migrating jets. This can also be shown to be true when we vertically integrate to obtain equation 5.15.

In Figure 7.2, once again, the zonal flow anomalies are shown, but this time, with only the horizontal EP flux plotted. In phases A, B and C, the amplitude of the anomalous eddy momentum flux is stronger on the equatorward flank of the secondary jets. With a stronger forcing on the equatorward side, the zonal jets will migrate equatorward.

Under this idealized setup, we speculate the likely reason for the asymmetries associated with the convergence of $[u'v']$ fluxes can be attributed to the index of refraction values increasing near the equator. Waves generally propagate into regions of larger positive refractive index (e.g. Matsuno 1970). Since the interior of the fluid is roughly homogenized (the PV gradient is small), the index of refraction is larger near the equator and hence, the Rossby wave propagation is favored on the equatorward side.

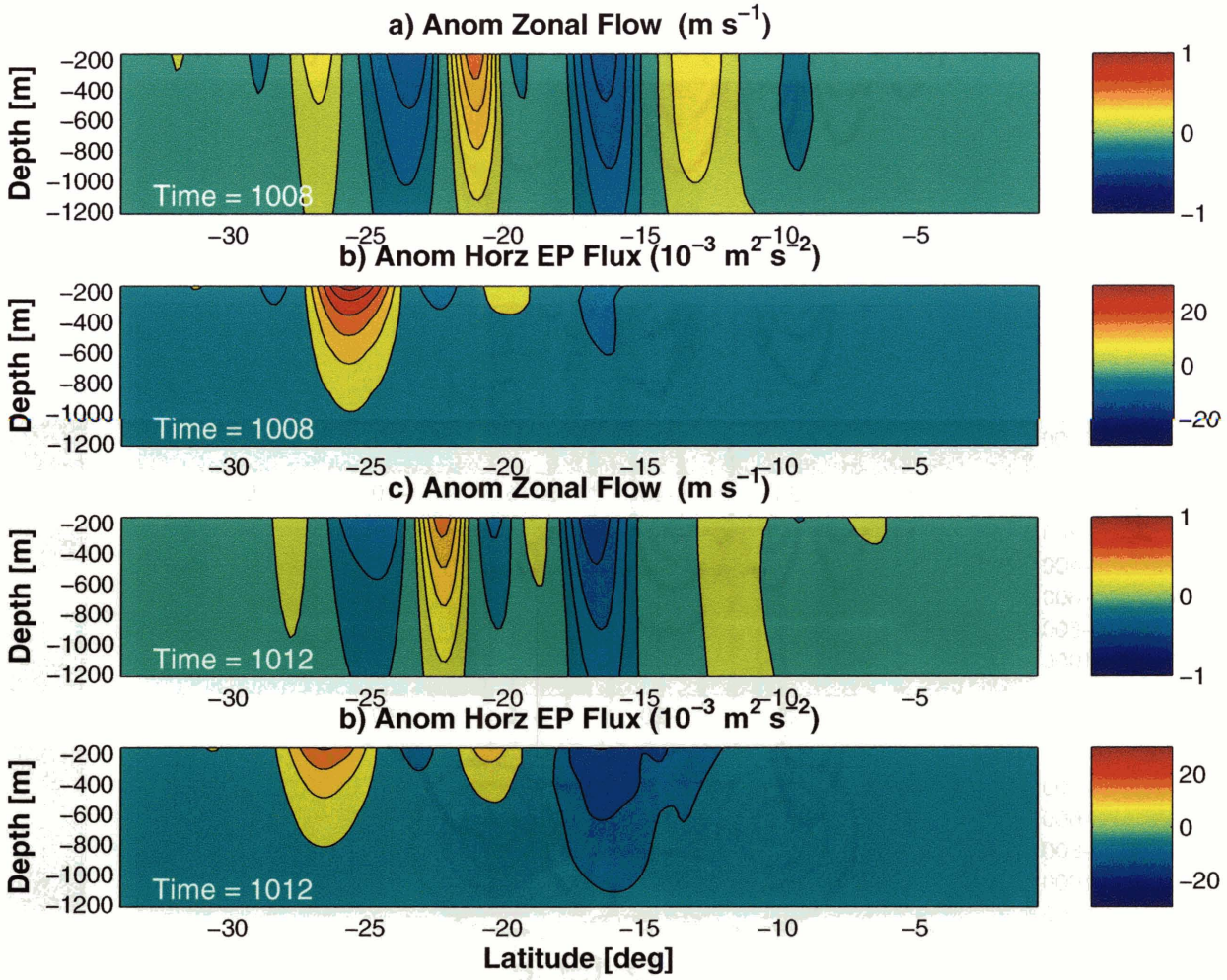

Figure 7.1: A snapshot of a) zonal anomalies and b) of the anomalous horizontal EP flux at t = 1008 years. A snapshot of c) zonal anomalies and d) of the anomalous horizontal EP flux at t = 1012 years.

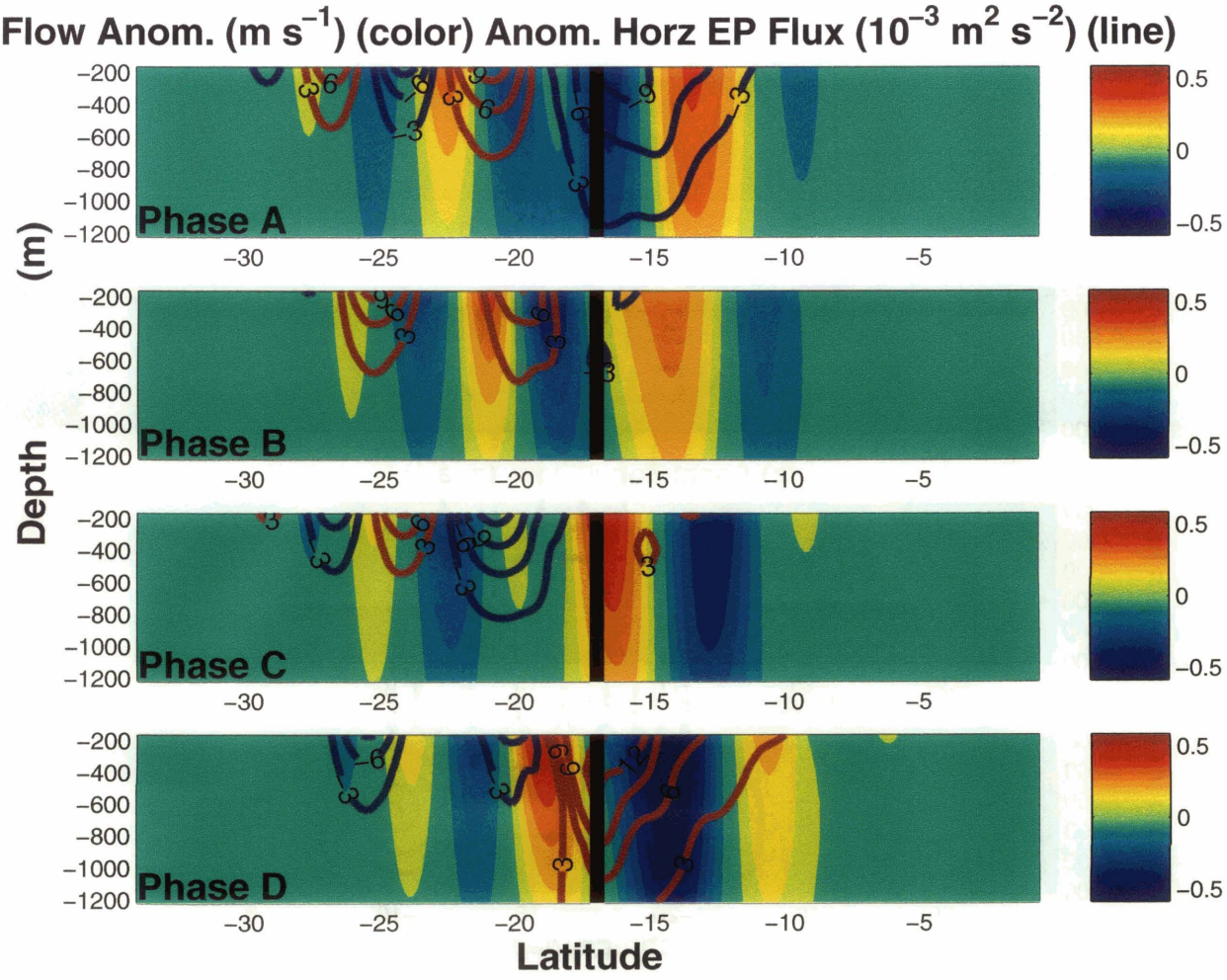

Figure 7.2: Anomalous horizontal EP flux (line) for each EOF phase plotted over zonally-averaged zonal flow anomalies (in color).

In terms of the PV gradient, this is somewhat similar to the analyses of the atmosphere, where interior gradients are near zero and the largest values are near the upper boundary. As we have shown from our results, given such a setup, zonal anomalies propagate equatorward. However, an observational study by Feldstein (1998) have demonstrated that in the real atmosphere, zonal anomalies actually propagate poleward. To the author's knowledge, no theory has been suggested to describe this phenomenon. But in any case, any convincing mechanism would most likely need to counteract the argument where in regions of homogenized PV, the index of refraction will have an equatorward bias leading to asymmetrical wave propagation.

We conclude this section by discussing why migrating jets were observed in this particular study and not others (e.g. Panetta 1993). Even in this study, the primary jet did not migrate. Lee (2005) who modelled multiple jets on a sphere may have had a hint of migrating jets (see Fig 3b in Lee 2005), but for the most part, jets were steady. As discussed above, what makes the zonal anomalies migrate equatorward arises from larger values of the index of refractions with respect to the region of the instability. This leads to Rossby waves propagating more "efficiently" equatorward and providing a bias in the convergence of the eddy momentum flux.

However, the above argument holds only, for the most part, in the presence of weak PV gradients. In the absence of PV homogenization, if PV gradients are sufficiently large, they will dominate over the spherical terms in the refractive index, and Rossby waves may not necessarily propagate more efficiently on the equatorward flanks. For the primary jet,

the PV gradient is not weak (see Fig 3.2). The index of refraction is no longer necessarily larger on the equatorward side of the instability, and hence the jet only "wobbles" from its time-mean location.

7.2 Zonal index variability

A time series of the zonal-mean zonal flow shows the primary jet "wobbling" as a distinct feature. An EOF analysis shows that this jet's meridional displacement is the leading mode of variability. Since the model-imposed forcings are constant in time, the internal dynamics is likely the cause for this mode.

A mechanism for creating this variability is the eddy-zonal flow feedback (LH01). Eddies drive changes to the zonal-mean state, which then correspond (presumably later in time) with changes in eddy activity. Using this framework, we examine the variability of the zonal index.

As discussed in section 5.2, there are distinct differences in the eddy activity between the high and low zonal index. Figure 5.1 shows in the region of the primary jet, in the high and low zonal indexes, both are dominated by upward wave activity propagation; however stronger upward wave activity is associated with the high zonal index. In terms of latitudinal wave propagation, once again, it's the high zonal index that shows the greatest wave activity. In the low index, Phase A shows weak wave activity equatorward of the time-mean location of the jet, while for Phase B, its the poleward side that is weak. But in any case, for all phases, the eddy forcing acts to accelerate the mean flow near the location of the primary

jet. The primary difference is that in the high index, the eddy forcing is stronger.

Figure 7.3 shows the vertically-integrated total eddy forcing for both the high and low zonal index. In the high index, it is no surprise that the vertically-integrated eddy forcing is much greater than in the low index. In addition, the peak of the eddy forcing has shifted latitudinally one degree poleward. Therefore, the jet responds by displacing poleward, consistent with how we defined the high zonal index.

This poleward bias in the eddy forcing can be attributed to the secondary jets migrating into the poleward flank of the primary jet. As it enters on the southward side, the positive zonal anomalies will produce a region of anomalously positive baroclinicity. As described in section 5.2, this will lead to a positive eddy forcing, accelerating the jet's poleward flank and "shifting" the jet poleward.

By eddies driving changes to the mean state, this so far is consistent with the proposed eddy feedback. We now see if the changes in the mean state correspond with changes in the eddy activity favorable to sustain the annular modes.

Prior to the onset of the low index, through baroclinic instability, the vertical shear has been reduced right at the jet as shown by the negative zonal flow anomalies in Phase A (see Figure 5.2). So during the low index, this induces an anomalously negative eddy forcing, and therefore the largest (total) eddy forcing is now equatorward of the jet's time-mean position as shown in Figure 7.3.

This shows that eddies have driven changes in the mean state such that the eddy activity has been displaced and favorable in the perpetuation of the annular modes.

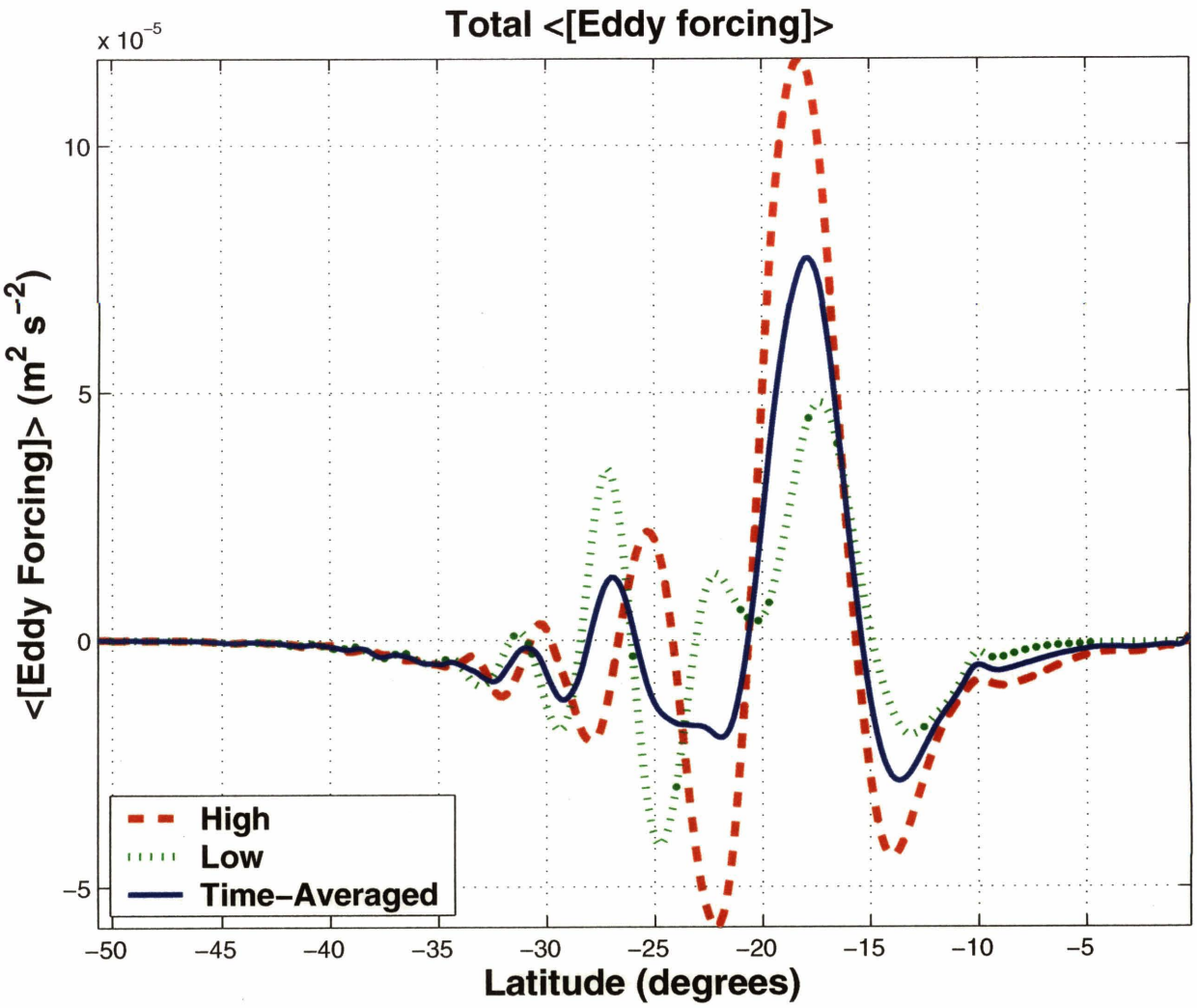

Figure 7.3: Total eddy forcing for the high and low zonal index. As reference, the time-averaged total eddy forcing is also plotted.

Chapter 8

Conclusion

Results from our model show the leading mode of the zonally-averaged zonal flow variability is an equivalent barotropic structure with largest anomalies three degrees north and south of the jet's time-averaged location. Physically, this represents the meridional displacement of the jet. The primary forcing in this leading mode of variability is associated with the anomalous eddy momentum flux, which ultimately drives changes to the zonal index variability.

An analysis of the time-averaged momentum budget shows that the primary jet is eddy-driven. The model's prescribed wind stress transfers momentum from the atmosphere into the ocean. Eddies then transfer momentum downward and equatorward. The vertical transfer of momentum eventually gets removed from the system by the bottom drag. The time-averaged latitudinal momentum flux converges at the location of the primary jet and sustains the jet despite the presence of frictional forces.

There is a meridional asymmetry in the index of refraction in the regions of the migrating jets owing to sphericity effects and homogenization of the interior PV. Larger values are on

the equatorward side of the wave activity source. Since the secondary jets are baroclinically unstable, baroclinic waves will be generated and will propagate away and provide momentum fluxes into the jet. However, because of the higher values, the index of refraction promotes propagation on the equatorward side more favorably. Therefore the eddy momentum fluxes and its associated convergence will be stronger on the equatorward side causing the jets to migrate equatorward.

The role played by friction is not negligible. Where the zonal flow is strongest, friction attains its maximum value and opposes any eddy forcing that could have accelerated the flow. Instead, positive flow tendency occurs where the zonal flow is weak (thus, friction is also weak) while the forcing is still prevalent. Therefore, the flow accelerates on the flanks of the jet.

Since the secondary jets migrate towards and into the primary jet, the associated zonally-averaged zonal flow anomalies will affect the zonal index and its leading mode of variability. As the secondary jet approaches the poleward flank of the primary jet, anomalously positive eddy forcing leads to the jet being meridionally displaced poleward. During this high index phase, the anomalously positive vertical shear results in stronger baroclinic instability at the jet transporting even more momentum downward, until some point where the eddy heat flux, which acts downgradient, turns the vertical shear anomalously negative. This in turn, causes the eddy forcing to be anomalously negative poleward of the time-mean position of the jet. Therefore, the strongest (total) eddy forcing now appears equatorward of the jet causing the jet to "shift" back equatorward. At some point, the systematic migration of

zonal flow anomalies will once again migrate into the primary jet repeating the sequence of events and sustaining this leading mode of variability.

8.1 Future Work

We have shown that migrating jets are possible when eddies homogenize the interior potential vorticity and when the sphericity of the earth is captured. However, on a β-plane, assuming the basic state flow is zero, there would be no latitudinal variations of the refractive index. In theory, the refractive index can be changed by contriving a mean flow such that meridional biases in the refractive index would allow for zonal anomalies to propagate similar to the processes seen here. It would be interesting, if possible, to create a mean flow similar to our setup where secondary weaker jets migrate towards a primary jet, a region of high PV gradient. Furthermore, can these baroclinically unstable weaker jets migrate towards the primary jet from both the poleward and equatorward flanks? Additionally, having confirmed the possibility of migrating jets poleward of the primary jet, under a similar setup on a sphere and "moving" the primary jet's position more poleward, the possibility of migrating jets on the equatorward flank of the primary jet has yet to be studied.

In regards to the meridional displacement of the jet, increased wave activity was associated with the high zonal index, while weak eddy activity was observed for the low zonal index, and perhaps as a consequence, periods associated with the onset of the low zonal index lasted for longer durations. For our 313-year model study, Phase A constituted 95 years in total, nearly twenty percent more than any other phase. Using an aquaplanet GCM,

Feldstein and Lee (1996) found similar results, where the weaker eddy activity occurred during the low zonal index and lasted for longer durations. Understanding what controls the time-scale pertaining to why certain phases last longer than others may have implications for extended-range weather forecasts.

Appendix A

Reconstructing zonal flow

The zonally-averaged zonal flow, u can be split into the time-mean $u(\bar{y}, z)$ and the anomalies $u'(y, z, t)$. The purpose of undertaking an empirical orthogonal function (EOF) analysis was to capture the spatial and temporal variability associated with u'.

$$u' = u'(y, z, t) = \sum_{n}^{k=\infty} f_n(t) \cdot V_n(y, z) \tag{A.1}$$

where f is the phase and amplitude of the spatial pattern, V, where n denotes the nth eigenvector. In the literature, f is often called the principal component.

To obtain the time series of f for each eigenvector, we multiply by the mth eigenvector to both sides and integrate through the domain.

$$\int\int u' \cdot V_m d\phi dz = \int\int \sum_{n}^{\infty} f_n(t) \cdot V_n \cdot V_m d\phi dz \tag{A.2}$$

Since eigenvectors are orthogonal, then the right hand side of A.2 is equal to zero unless V_n=V_m. Therefore, changing he subscripts from m to n (since they are the same), we obtain

$$f_n(t) = \frac{\int\int u' \cdot V_n d\phi dz}{\int\int V_n^2 \cdot d\phi dz} \tag{A.3}$$

In Figure 4.4, we have used A.1 where $k = 2$ and added the time-averaged zonal flow to obtain the time series of the reconstructed zonally-averaged zonal flow.

Bibliography

Andrews, D. G., J. R. Holton, and C. B. Leovy, 1987: *Middle Atmosphere Dynamics.* Academic, London.

Chen, P. and W. A. Robinson, 1992: Propagation of planetary waves between the troposphere and stratosphere. *J. Atmos. Sci.*, **49**, 2533–2545.

Eady, E. T., 1949: Long waves and cyclone waves. *Tellus*, **1**, 35–52.

Edmon Jr., H. J., B. J. Hoskins, and M. E. McIntyre, 1980: Eliassen-Palm cross-sections for the troposphere. *J. Atmos. Sci.*, **37**, 2600–2615.

Feldstein, S., 1998: An observational study of the intraseasonal poleward propagation of zonal mean flow anomalies. *J. Atmos. Sci.*, **55**, 2516–2529.

Feldstein, S. and S. Lee, 1996: Mechanisms of zonal index variability in an aquaplanet GCM. *J. Atmos. Sci.*, **53**, 3541–3556.

Held, I. and D. G. Andrews, 1983: On the direction of the eddy momentum flux in baroclinic instability. *J. Atmos. Sci.*, **40**, 2220–2231.

Held, I. and V. D. Larichev, 1996: A scaling theory for horizontally homogeneous, baroclinically unstable flow on a beta-plane. *J. Atmos. Sci.*, **53**, 946–952.

Hurrell, J. W., 1995: Decadal trends in the North Atlantic Oscillation regional temperatures and precipitation. *Science*, **269**, 676–679.

Lee, S., 2005: Baroclinic multiple zonal jets on the sphere. *J. Atmos. Sci.*, **62**, 2484–2498.

Limpasuvan, V. and D. L. Hartmann, 2000: Wave-maintained annular modes of climate variability.

Lorenz, D. J. and D. L. Hartmann, 2001: Eddy-zonal flow feedback in the Southern Hemisphere. *J. Atmos. Sci.*, **58**, 3312–3327.

Lorenz, E. N., 1951: Seasonal and irregular variations of the northern hemisphere sea-level pressure profile. *J. Meteor*, **8**, 52–59.

Marshall, J., A. Adcroft, C. Hill, L. Perelman, and C. Heisey, 1997: A finite-volume, incompressible Navier Stokes model for studies of the ocean on parallel computers. *J. Geophys. Res.*, **102**, 5753–5766.

Marshall, J., C. Hill, L. Perelman, and A. Adcroft, 1997: Hydrostatic, quasi-hydrostatic, and nonhydrostatic ocean modeling. *J. Geophys. Res.*, **102**, 5733–5752.

Matsuno, T., 1970: Vertical propagation of stationary planetary waves in the winter Northern Hemisphere. *J. Atmos. Sci.*, **27**, 871–883.

Nakamura, M. and R. A. Plumb, 1994: The effects of flow asymmetry on the direction of Rossby wave breaking. *J. Atmos. Sci.*, **51**, 2031–2045.

Namias, J., 1950: The index cycle and its role in the general circulation. *J. Meteor.*, **7**, 130–139.

North, G. R., T. L. Bell, R. F. Cahalan, and F. J. Moeng, 1982: Sampling errors in the estimation of empirical orthogonal functions. **110**, 699–706.

Panetta, R. L., 1993: Zonal jets in wide baroclinically unstable regions: persistence and scale selection. *J. Atmos. Sci.*, **50**, 2073–2106.

Pedlosky, J., 1987: *Geophysical Fluid Dynamics.* Springer-Verlag, second edition.

Rhines, P. B., 1975: Waves and turbulence on a beta-plane. *J. Fluid Mech.*, **69**, 417–443.

Rossby, C. G., 1939: Relations between variations in the intensity of the zonal circulation and the displacements of the semi-permanent centers of action. *J. Mar. Res*, **2**, 38–55.

Thompson, D. W. J. and J. M. Wallace, 1998: The Arctic Oscillation signature in the wintertime geopotential height fields. **25**, 1297–1300.

Thompson, D. W. J. and J. M. Wallace, 2000: Annular modes in the extratropical circulation. Part I: Month-to-month variability. **13**, 1000–1016.

Treguier, A. M. and R. L. Panetta, 1994: Multiple zonal jets in a quasigeostrophic model of the Antarctic Circumpolar Current. *J. Phys. Oceanogr.*, **24**, 2263–2277.

Vallis, G. K. and M. E. Maltrud, 1993: Generation of mean flows and jets on a beta plane and over topography. *J. Phys. Oceanogr.*, **23**, 1346–1362.

Walker, G. T. and E. W. Bliss, 1932: World weather V memoirs. *Roy. Meteor. Soc.*, **4**, 53–84.

Whitaker, J. S. and C. Snyder, 1993: The effects of spherical geometry on the evolution of baroclinic waves. *J. Atmos. Sci.*, **50**, 597–612.

Williams, G., 1978: Planetary circulations: 1. Barotropic representation of Jovian and terrestrial turbulence. *J. Atmos. Sci.*, **35**, 1399–1426.

Yu, J.-Y. and D. L. Hartmann, 1993: Zonal flow vacillation eddy forcing in a simple GCM of the atmosphere. *J. Atmos. Sci.*, **50**, 3244–3259.